

**Infragravity Waves over Topography:
Generation, Dissipation, and Reflection**

by

James M. Thomson

Submitted to the Joint Program in Physical Oceanography
in partial fulfillment of the requirements for the degree of

Doctor of Philosophy

at the

MASSACHUSETTS INSTITUTE OF TECHNOLOGY

and the

WOODS HOLE OCEANOGRAPHIC INSTITUTION

September 2006

©WHOI, 2006. All rights reserved.

Author
Joint Program in Physical Oceanography
August 16, 2006

Certified by
Steve Elgar
Senior Scientist, WHOI
Thesis Supervisor

Accepted by
Joseph Pedlosky
Chairman, Joint Committee for Physical Oceanography

Infragravity Waves over Topography: Generation, Dissipation, and Reflection

by

James M. Thomson

Submitted to the Joint Program in Physical Oceanography
on August 16, 2006, in partial fulfillment of the
requirements for the degree of
Doctor of Philosophy

Abstract

Ocean surface infragravity waves (periods from 20 to 200 s) observed along the southern California coast are shown to be sensitive to the bottom topography of the shelf region, where propagation is linear, and of the nearshore region, where nonlinearity is important. Infragravity waves exchange energy with swell and wind waves (periods from 5 to 20 s) via conservative nonlinear interactions that approach resonance with decreasing water depth. Consistent with previous results, it is shown here that as waves shoal into water less than a few meters deep, energy is transferred from swell to infragravity waves. In addition, it is shown here that the apparent dissipation of infragravity energy observed in the surfzone is the result of nonlinear energy transfers from infragravity waves back to swell and wind waves. The energy transfers are sensitive to the shallow water bottom topography. On nonplanar beach profiles the transfers, and thus the amount of infragravity energy available for reflection from the shoreline, change with the tide, resulting in the tidal modulation of infragravity energy observed in bottom-pressure records on the continental shelf. The observed wave propagation over the shelf topography is dominated by refraction, and the observed partial reflection from, and transmission across, a steep-walled submarine canyon is consistent with long-wave theory. A generalized regional model incorporating these results predicts the observed infragravity wave amplitudes over variable bottom topography.

Thesis Supervisor: Steve Elgar
Title: Senior Scientist, WHOI

Acknowledgments

I thank the Office of Naval Research (Coastal Geosciences Program, N00014-02-10145), the National Science Foundation (Physical Oceanography, OCE-0115850), and the Academic Programs office at WHOI for their generous support.

My advisor, Dr. Steve Elgar, has contributed tirelessly to this work and to my professional development. He has taught, challenged, and encouraged me in an apprenticeship beyond my highest expectations.

Committee members and coauthors, Drs. David Chapman, Robert Guza, Thomas Herbers, Steve Lentz, Joseph Pedlosky, Britt Raubenheimer, and Carl Wunsch, have patiently advised, contributed, questioned, and listened. I am grateful for their collaborations and instruction.

The field observations were made possible by many dedicated professionals at WHOI, the Scripps Institute of Oceanography, the Naval Postgraduate School, and Ohio State University. Of the many contributions, Peter Schultz's efforts have been paramount. I am proud of the work we have done together, and I am grateful for his expertise, enthusiasm, and friendship.

I also thank Alex Apotsos, Melanie Fewings, Greg Gerbi, Carlos Moffat, Andrew Mosedale, Dave Sutherland, and my other peers in the Joint Program who have enhanced my experience and education greatly.

Many thanks go to my family as well, who always have encouraged me to work hard and enjoy what I do.

And my gracious wife, Jess, I will be thanking for a long, long time. She has fed hungry fieldcrews, braved the many uncertainties of these five years, encouraged every small bit of progress, and provided a source of calmness and levity to each of my days. Many new things are in our future together, and I look forward to all of them.

Contents

1	Introduction	11
1.1	Thesis Outline	12
1.2	Background	12
1.3	The Nearshore Canyon Experiment	16
2	Tidal Modulation of Infragravity Waves via Nonlinear Energy Losses in the Surfzone	23
2.1	Introduction	24
2.2	Field Observations	26
2.3	Analysis	28
2.3.1	Nonlinear Energy Balance	29
2.3.2	Numerical Model	32
2.3.3	Bottom Profile Dependence	34
2.4	Conclusions	34
3	Reflection and tunneling of ocean waves observed at a submarine canyon	41
3.1	Introduction	42
3.2	Theory	42
3.3	Field Observations	48
3.4	Methods	49

3.5	Results	52
3.6	Conclusions	55
4	Conclusions and Regional Description	59
4.1	Shoaling and Unshoaling	59
4.2	Refraction and Canyon Reflections	60
4.2.1	Case Study	64
4.2.2	Climatology	66
4.2.3	Model Skill	66
4.3	Suggested Applications	69

List of Figures

1-1	Infragravity schematic	13
1-2	Example energy spectra	15
1-3	Nearshore Canyon Experiment array and bathymetry	17
1-4	Nearshore Canyon Experiment data summary	19
2-1	Example of tidal modulation	25
2-2	Cross-shore energy flux profiles	27
2-3	Nonlinear exchange in the surfzone	31
2-4	Cross-shore evolution of biphasic	33
2-5	Bottom profile dependence at all transects	35
3-1	Detailed bathymetry at La Jolla canyon	43
3-2	Reflection coefficients versus frequency	45
3-3	Schematic of reflection and tunneling	47
3-4	Phase shift during reflection	54
4-1	Infragravity shoaling dominated by free waves	61
4-2	Example ray paths using refraction-reflection model	63
4-3	Case study of infragravity variance along isobaths	65
4-4	Average infragravity variance along isobaths	67
4-5	Refraction model-data comparison	68

Chapter 1

Introduction

Infragravity waves are oscillatory motions of the ocean surface with periods of order one minute. These waves are strongest near the shoreline [*Guza and Thornton, 1985*], where usually they are coupled to higher frequency surface motions (swell and wind waves) [*Elgar et al., 1992*]. Most observations of infragravity waves have been in regions with gently varying bottom topography [*Herbers et al., 1995b*]. Here, infragravity waves propagating over rapidly varying topography are investigated using field observations, analytic theories, and numerical models. The specific objectives are to:

- identify the sources and sinks of infragravity motions,
- determine the cause of a tidal modulation of infragravity energy observed at offshore locations, and
- test a long-wave prediction for the reflection and transmission of infragravity waves from a steep-walled submarine canyon.

The results are generalized to formulate a descriptive regional model. Although a full scale modeling effort is beyond the scope of the thesis, the results identify the processes that should be included to model infragravity waves accurately, and indicate several possible improvements to existing models.

1.1 Thesis Outline

Background information on infragravity waves, a review of previous work, and general information regarding the field data collection are presented in Chapter 1. Results from detailed process studies are presented as independent articles (i.e., separate abstracts and bibliographies) in Chapters 2 and 3.

Chapter 2, “Tidal Modulation of Infragravity Waves via Nonlinear Energy Losses in the Surfzone,” is an extension of Thomson et al. [2006], and demonstrates that infragravity wave energy is transferred to swell and wind waves in the surfzone, in contrast with the well-known transfer of energy to infragravity waves from swell and wind waves via nonlinear interactions in deeper water. This energy loss is enhanced over the low tide beach profile, resulting in the tidal modulation of infragravity energy observed offshore.

Chapter 3, “Reflection and Tunneling of Ocean Waves Observed at a Submarine Canyon,” is an extension of Thomson et al. [2005], including a detailed methods section published online only, and describes the observational validation of a long-wave theory for the partial reflection and transmission of infragravity waves at a steep-walled submarine canyon.

Chapter 4 summarizes the results and suggests a descriptive model for the regional distribution of infragravity energy based on the results in the previous chapters.

1.2 Background

Infragravity waves (surface gravity waves with periods of 20 to 200 s) were first observed as a “surf beat” modulation coincident with groups of narrow-banded swell (periods of 10 to 20 s) and having the period and wavelength (~ 500 m) of the groups (Figure 1-1) [Munk, 1949, Tucker, 1950]. Subsequent investigations have shown that these waves are important to alongshore currents in the surfzone [Sasaki, 1976], sediment transport near the shoreline [Bauer and Greenwood, 1990], oscillations in har-

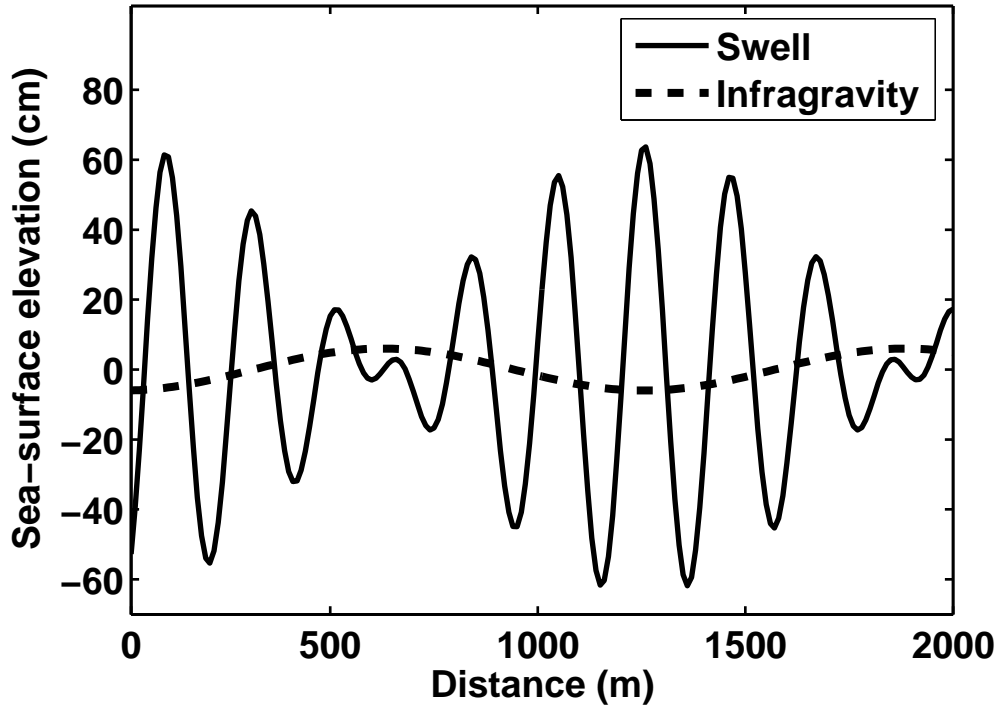


Figure 1-1: Sea-surface elevation versus distance showing a group modulation in swell (periods from 10 to 20 s) waves (solid curve) and the accompanying forced infragravity (period from 20 to 200 s) wave (dashed curve). Group modulations are caused by the beating of neighboring frequencies, and the resulting infragravity wave is forced at the corresponding difference, or beat, frequency. In deep water, the forced infragravity wave remains small (amplitudes of a few cm). In shallow water, the forcing is near-resonant and large (1 m) amplitude infragravity waves can occur.

bors [Okiihiro *et al.*, 1993], and fluctuations in seismic records [Dolenc *et al.*, 2005].

In deep water, nonresonant nonlinear quadratic interactions between swell waves produce forced infragravity motions [Hasselmann, 1962]. Using a slowly varying (WKBJ) approach in finite depth, this forcing can be expressed as excess momentum flux owing to the swell groups [Longuet-Higgins and Stewart, 1962], and is consistent with observations [Elgar *et al.*, 1992, Herbers *et al.*, 1994]. As waves enter shallow water, the quadratic nonlinear interactions approach resonance, and in water less than a few meters deep significant energy can be transferred from wind waves to infragravity motions over a few hundred meters of propagation [Gallagher, 1971, Elgar and

Guza, 1985, Herbers et al., 1995b, Ruessink et al., 1998; and others]. Thus, energy at infragravity periods usually is low in the deep ocean and increases as water depth decreases, reaching amplitudes up to 1 m at the shoreline (Figure 1-2).

When the swell waves break and dissipate in the surfzone, the infragravity waves are released and propagate towards the shoreline as free waves [*Herbers et al., 1995a*]. Recent analysis suggests that in the surfzone infragravity waves transfer some energy back to higher frequencies [*Thomson et al., 2006, Henderson et al., submitted, 2006*], before reflecting from the shoreline [*Suhayda, 1974, Guza and Thornton, 1985, Nelson and Gonsalves, 1990, Elgar et al., 1994, Sheremet et al., 2002*]. Reflected infragravity waves can be refractively trapped (i.e., edge waves) close to the shore in a topographic wave guide [*Eckart, 1951, Huntley et al., 1981, Oltman-Shay and Guza, 1987; and others*] or can propagate to deep water obeying the linear finite depth dispersion relation

$$\omega^2 = gk \tanh kh, \quad (1.1)$$

where ω is the radian frequency, g is the gravitational acceleration, k is the wavenumber, and h is the water depth [*Mei, 1989, §1.4*]. Infragravity energy levels observed seaward of the turning point for edge waves are dominated by free waves (i.e., leaky waves) and characterized by broad frequency-directional spectra [*Elgar et al., 1992, Herbers et al., 1995a*].

Previous investigations of infragravity waves have focused on regions with along-shore homogeneous bathymetry. Consequently, the possible affects of rapidly varying topography on infragravity wave propagation were untested [*Holman and Bowen, 1984*] prior to the recent observation of infragravity reflection and transmission at a submarine canyon [*Thomson et al., 2005*]. By incorporating the observed strong reflections into standard ray tracing techniques, and applying a conservative nonlinear energy balance [*Thomson et al., 2006*], predictive models for infragravity waves can be improved.

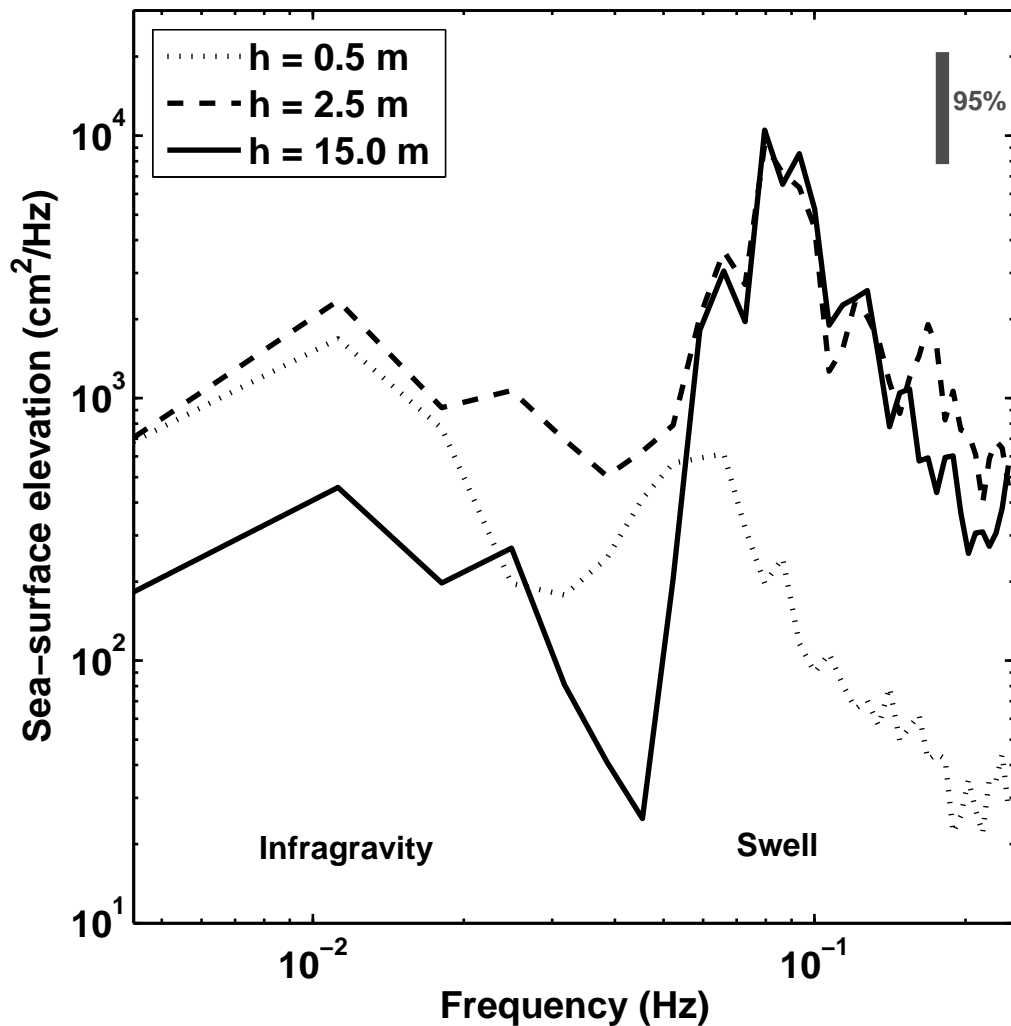


Figure 1-2: Spectral energy density of sea-surface elevation (cm^2/Hz) versus frequency (Hz) from $h = 15.0$ (solid curve), 2.5 (dashed curve), and 0.5 m (dotted curve) water depths observed on November 10, 2003 at 2100 hrs PST. This example of spectral evolution shows the well-known growth at infragravity frequencies (0.005 to 0.05 Hz) with decreasing water depths, as well as the dissipation owing to breaking at swell and wind frequencies (0.05 to 0.2 Hz) in shallow water (depths less than 2.5 m), such that infragravity motions dominate the spectrum in the shallowest depth (dotted curve). The 95% confidence interval, based on a χ^2 distribution with 42 degrees of freedom [Priestley, 1981], is shown in the upper right corner.

1.3 The Nearshore Canyon Experiment

Data used in this thesis were collected as part of the Nearshore Canyon Experiment (NCEX) during the fall of 2003. Specific information regarding data and methods is presented within Chapters 2, 3, and 4. This section presents additional information.

An array of bottom-mounted current meters and pressure gages was maintained along the southern California coast from September to December, 2003 (Figure 1-3). The NCEX array was designed to study waves and currents near and onshore of two steep submarine canyons. Additional instruments were deployed to study nonlinear wave evolution (Chapter 2) across the surfzone and nearshore region at the northern end of the array ($y = 2.7$ km, Figure 1-3), and to study partial wave reflection (Chapter 3) from La Jolla canyon ($y \approx -1.0$ km, Figure 1-3). The data include a range of wave (Figure 1-4) and atmospheric (not shown) conditions.

Colocated pressure and velocity data were collected hourly at 2 Hz for 3072 s (51 min), although for a three-week period some data were collected at 16 Hz and then subsampled to 2 Hz during the analysis. Setra pressure gages without colocated velocity measurements sampled continuously at 2 Hz throughout the experiment, interrupted by one (or two for some instruments) turn-arounds. In depths greater than 3 m, the colocated current meters (SonTek and NorTek acoustic Doppler velocimeters) and pressure gages (ParoScientific and Druk resonant pressure transducers) were mounted on fixed platforms within 1 m of the seafloor. In depths less than 3 m, the pressure gages were buried up to 1 m to prevent flow noise [Raubenheimer *et al.*, 1998]. After initial quality control to remove bad data, power spectra of pressure and each of the three velocity components were calculated by subdividing the 3072 s records into 1024 s windows with 75% overlap between adjacent windows, Fourier transforming the data, and merging every seven neighboring frequency bands. The resulting spectral values have 42 degrees of freedom [Priestley, 1981], and are corrected for attenuation by the water column using linear finite depth theory (i.e., attenuation is assumed to be proportional to $\cosh(kh)$ [Mei, 1989, §1.4]). In a test with two inde-

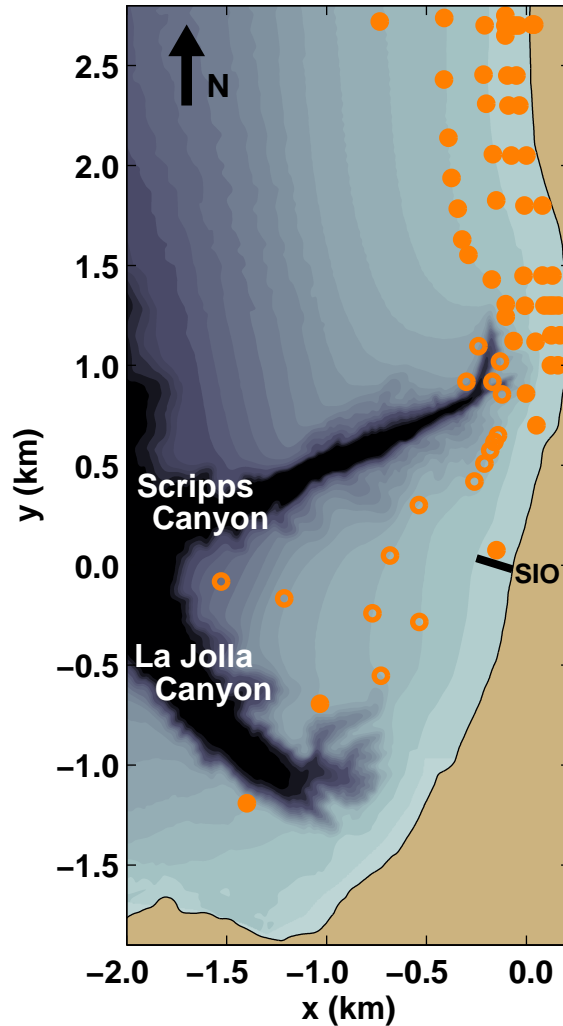


Figure 1-3: Nearshore Canyon Experiment instrument array (symbols) and bathymetry (shaded surface) using a local coordinate system (origin at the foot of the Scripps pier: 32.866° N, -117.256° W) along the southern California coast (tan region). Bottom mounted instruments measured pressure (open symbols), and pressure colocated with velocity (filled symbols) for two months during the fall of 2003. Water depths range from over 100 m (dark regions) in the Scripps (northern) and La Jolla (southern) canyons to 0 m at the shoreline (boundary between the light blue shading and tan region).

pendent instruments deployed at the same location, the cross-spectra of pressure and velocity from the two instruments were coherent above the 99.9% confidence level in the frequency bands of interest (0.005 to 0.25 Hz).

Offshore bathymetry (Figure 1-3) was surveyed using shipboard acoustic equipment prior to the experiment. Nearshore bathymetry was surveyed both prior to, and weekly during, the experiment using a customized personal watercraft equipped with a Differential Global Positioning System (DGPS), gryoscope, and sonar transducer. In addition, the acoustic current meters in less than 3 m depth estimated the distance to the slowly changing seafloor every hour. The offshore bathymetry has vertical errors of ± 10 cm and horizontal errors of ± 50 cm. The nearshore bathymetry has vertical errors of ± 10 cm and horizontal errors of ± 5 cm. Changes in nearshore bathymetry observed during the experiment were not sufficient to alter the results of the nearshore study (Chapter 2), and thus a single survey from October was used throughout the analysis.

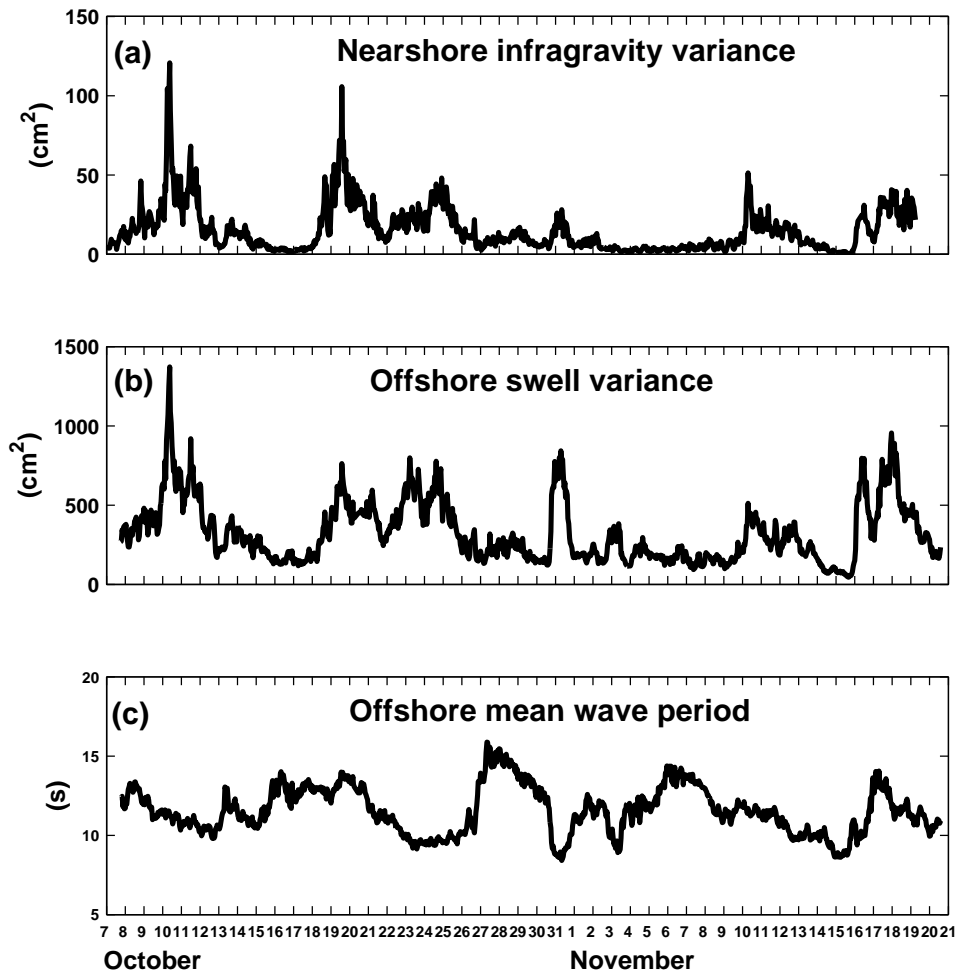


Figure 1-4: (a) Nearshore infragravity variance, (b) offshore swell variance, (c) and offshore mean wave period measured hourly at the northern transect ($y = 2.7$ km) versus time during the Nearshore Canyon Experiment. Chapter 2 uses data from October 25 to November 21, when additional instruments were deployed in the inner surfzone. Chapter 3 uses data from October 1 to October 15 and November 24 to December 8 (not shown), when instruments were deployed on either side of La Jolla Canyon. Chapter 4 uses averages from the entire two-months of data, and thereby includes the full range of wave conditions. The mean wave period was calculated as the weighted (by energy) average period of hourly pressure spectra (i.e., the period corresponds to the centroid of the energy spectrum), after correcting for water depth attenuation. The nearshore data (a) are from instruments in approximately 2.5 m water-depth, and the offshore data (b and c) are from instruments in approximately 15 m water-depth.

Bibliography

- Dolenc, D., B. Romanowicz, D. Stakes, P. McGill, and D. Neuhausser (2005), Observations of infragravity waves at the Monterey ocean bottom broadband station (MOBB), *Geochem. Geophys. Geosys.*, 6 (9), Q09002, doi:10.1029/2005GC000988.
- Elgar, S., T.H.C. Herbers, and R.T. Guza (1994), Reflection of ocean surface gravity waves from a natural beach, *J. Phys. Oceanogr.*, 24, 1503-1511.
- Elgar, S., T.H.C. Herbers, M. Okihiro, J. Oltman-Shay, and R.T. Guza (1992), Observations of infragravity waves, *J. Phys. Oceanogr.*, 97, C10 15573-15577.
- Gallagher, B. (1971), Generation of surf beat by non-linear wave interactions, *J. Fluid Mech.*, 49, 1-20.
- Guza, R.T., and E.B. Thornton (1985), Observations of surf beat, *J. Phys. Oceanogr.*, 90, C2 3161-3172.
- Hasselmann, K. (1962), On the nonlinear energy transfer in a gravity-wave spectrum, 1, General theory, *J. Fluid Mech.*, 12, 481-500.
- Henderson, S.M., R.T. Guza, S. Elgar, T.H.C. Herbers, and A.J. Bowen, Nonlinear generation and loss of infragravity wave energy, *J. Geophys. Res.*, submitted, 2006.
- Herbers, T.H.C, S. Elgar, and R.T. Guza (1994), Infragravity-frequency (0.005-0.05 Hz) motions on the shelf, I, Forced waves, *J. Phys. Oceanogr.*, 24, 5, 917-927.
- Herbers, T.H.C, S. Elgar, and R.T. Guza (1995a), Infragravity-frequency (0.005-0.05 Hz) motions on the shelf, II, Free waves, *J. Phys. Oceanogr.*, 25, 6, 1063-1079.
- Herbers, T.H.C, S. Elgar, and R.T. Guza (1995b), Generation and propagation of infragravity waves, *J. Geophys. Res.*, 100, C12 24863-24872.

- Holman, R.A., and A.J. Bowen (1984) Longshore structure of infragravity motions, *J. Geophys. Res.*, *89*, 6446-6452.
- Huntley, D.A., R.T. Guza, and E.B. Thornton (1981), Field observations of surf beat, Part 1. Progressive edge waves, *J. Geophys. Res.*, *86*, 6451-6466.
- Longuet-Higgins, M.S. and R.W. Stewart (1962), Radiation stress and mass transport in surface gravity waves with application to surf beats, *J. Fluid Mech.*, *13*, 481-504.
- Mei, C.C. (1989), The Applied Dynamics of Ocean Surface Waves, *Adv. Series on Ocean Eng.*, *Vol 1*, World Scientific, New Jersey, 740 pp.
- Munk, W.H. (1949), Surf beats, *Transactions, Amer. Geophys. Union*, *30*, 6 849-854.
- Oltman-Shay, J. and R.T. Guza (1987), Infragravity edge wave observations on two California beaches, *J. Phys. Oceanogr.*, *17*, 644-663.
- Peregrine, D.H. (1967), Long waves on a beach, *J. Fluid Mech.*, *27*, 815-827.
- Priestley, M.B. (1981), *Spectral Analysis and Time Series*, Academic Press, San Diego, CA, 890 pp.
- Raubenheimer, B., S. Elgar, and R.T. Guza (1998), Estimating wave heights from pressure measured in sand bed, *J. Wtrwy., Port, Coast., and Oc. Engrg.*, *124*, 151-154.
- Thomson, J., S. Elgar, and T.H.C. Herbers (2005), Reflection and tunneling of ocean waves observed at a submarine canyon, *Geophys. Res. Lett.*, *32*, L10602, doi:10.1029/2005GL022834.
- Thomson, J., S. Elgar, B. Raubenheimer, T.H.C. Herbers, and R.T. Guza (2006), Tidal modulation of infragravity waves via nonlinear energy losses in the surf-zone, *Geophys. Res. Lett.*, *33*, L05601, doi:10.1029/2005GL025514.

Tucker, M. (1950), Surf beats: sea waves of 1 to 5 minute period, *Proc. Roy. Soc. Lon., A202*, 565-573.

Chapter 2

Tidal Modulation of Infragravity Waves via Nonlinear Energy Losses in the Surfzone

Parts of this chapter were reprinted with permission from:

Thomson, J., S. Elgar, B. Raubenheimer, T.H.C. Herbers, and R.T.Guza (2006),
Tidal modulation of infragravity waves via nonlinear energy losses in the surfzone,
Geophys. Res. Lett., **33**, L05601, doi:10.1029/2005GL025514.

Copyright 2006, *American Geophysical Union*.

Abstract

The strong tidal modulation of infragravity (20 to 200 s period) waves observed on the southern California shelf is shown to be the result of nonlinear transfers of energy from these low-frequency long waves to higher-frequency motions. The energy loss occurs in the surfzone, and is stronger as waves propagate over the convex low-tide beach profile than over the concave high-tide profile, resulting in a tidal modulation of seaward-radiated infragravity energy. Although previous studies have attributed infragravity energy losses in the surfzone to bottom drag and turbulence, theoretical estimates using both observations and numerical simulations suggest nonlinear transfers dominate. The observed beach profiles and energy transfers are similar along several km of the southern California coast, providing a mechanism for the tidal modulation of infragravity waves observed in bottom-pressure and seismic records on the continental shelf and in the deep ocean.

2.1 Introduction

Infragravity surface waves (periods between 20 and 200 s) are observed throughout the deep [Webb *et al.*, 1991] and coastal [Munk *et al.*, 1956, Tucker, 1950] oceans, and are strongest near the shoreline [Guza and Thornton, 1985, Elgar *et al.*, 1992, and many others], where they force circulation [Kobayashi and Karjadi, 1996] and transport sediment [Holman and Bowen, 1982]. Although infragravity motions complicate seismic monitoring [Dolenc *et al.*, 2005], they may be useful for tsunami detection [Rabinovich and Stephenson, 2004].

It is well known that infragravity motions are generated by nonlinear interactions between higher-frequency (periods between 5 and 20 s) swell and wind waves [Longuet-Higgins and Stewart, 1962, Herbers *et al.*, 1995b], but the causes of energy loss are not understood. Previous studies have attributed infragravity energy loss to bottom drag [Raubenheimer *et al.*, 1995, Henderson and Bowen, 2002] and to breaking [van Dongeren *et al.*, 2004].

Tidally-modulated infragravity motions have been observed on the inner-shelf [Okiihiro and Guza, 1995], and in regional seismic records [Dolenc *et al.*, 2005], possibly contributing to free oscillations of the Earth [Rhie and Romanowicz, 2004, Tanimoto, 2005]. The reduced infragravity energy observed at low tide has been hypothesized to originate near the shoreline, where tidal variations of the surfzone width and beach slope might affect infragravity generation, dissipation, or reflection [Okiihiro and Guza, 1995].

Here, new observations of a tidal modulation on the southern California coast (Figure 2-1) confirm a nearshore origin, and show that the primary cause is an enhancement of energy loss over the low-tide surfzone bottom profile. Infragravity energy is transferred to higher-frequency motions in the surfzone through near-resonant nonlinear interactions between triads of wave components (i.e., a reversal of the infragravity generation mechanism). These nonlinear transfers are sensitive to the surfzone bottom profile, and thus tidal sea level variations over the non-uniform beach pro-

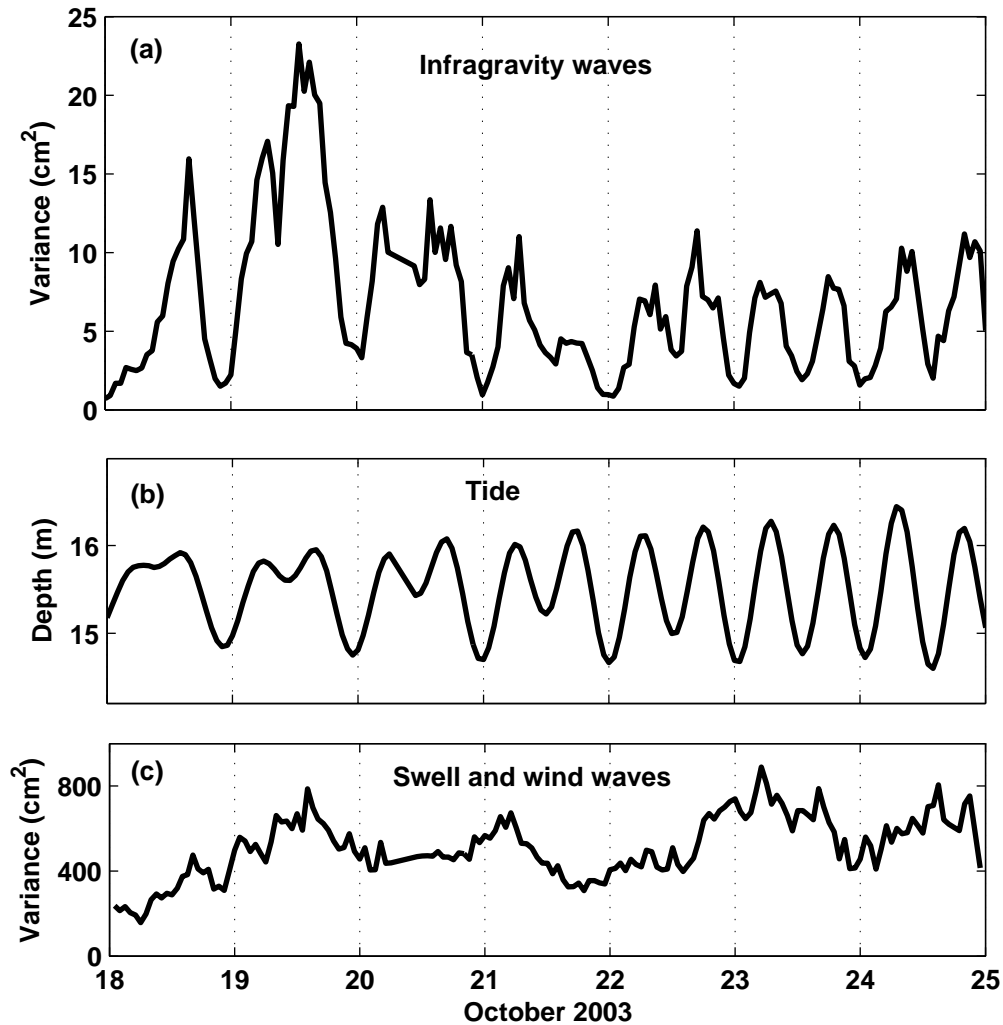


Figure 2-1: (a) Infragravity wave ($0.005 < f < 0.05$ Hz) variance (cm^2), (b) water depth (m), and (c) swell and wind wave ($0.05 < f < 0.25$ Hz) variance (cm^2) versus time. The hourly values are from a pressure gage mounted near the seafloor in 15-m water depth, 750 m from the shoreline on the southern California coast, 2.7 km north of the Scripps pier (Figure 1-3). The infragravity variance is correlated ($r^2 = 0.7$ for the data shown here, and $r^2 = 0.6$ for the 50-day period [Oct - Nov 2003]) and in phase with the diurnal and semi-diurnal tides, and is only weakly correlated ($r^2 = 0.3$ here and for all the data) with the variance of the swell and wind waves (although the correlation [$r^2 = 0.6$] with swell alone [$0.05 < f < 0.10$ Hz] is higher). Time series from the rest of the 50-day deployment are similar.

duce tidal changes in the infragravity energy observed offshore (Figure 2-1). Recent analysis of observations from a North Carolina beach also demonstrate nonlinear infragravity losses, but without a tidal modulation of infragravity energy [Henderson *et al.*, submitted, 2006].

2.2 Field Observations

Measurements of surface-wave-induced pressure and velocity were collected (at 2 Hz) along a cross-shore transect extending from 15-m water-depth to the shoreline near Torrey Pines State Beach in southern California (Figure 2-2c). Assuming shore-normal linear wave propagation in shallow water, shoreward (F^+) and seaward (F^-) infragravity energy fluxes were estimated from the observations of pressure (P) and cross-shore velocity (U) as [Sheremet *et al.*, 2002]

$$F^\pm = \frac{\sqrt{gh}}{4} \int \left(PP(f) + \left(\frac{h}{g}\right) UU(f) \pm \left(2\sqrt{\frac{h}{g}}\right) PU(f) \right) df, \quad (2.1)$$

where PP and UU are the auto-spectra of pressure and cross-shore velocity, respectively, PU is the cross-spectrum of pressure and cross-shore velocity, and the integral is over the infragravity frequency (f) range ($0.005 < f < 0.05$ Hz). In the linear, shallow-water approximation the group velocity is given by $C_g = \sqrt{gh}$, where g is gravitational acceleration and h is the water depth.

The infragravity variance of the 1-hr records observed in 15-m water depth (Figure 2-2c) is correlated with the tide (Figure 2-1). Averaged over the 50-day deployment, the infragravity variance at low tide was about 1/4 the variance at adjacent high tides, although larger modulations and other variability are present (e.g., October 19 and 20, Figure 2-1).

Infragravity wave energy can be trapped near the shore as low-mode edge waves [Huntley *et al.*, 1981, Oltman-Shay and Guza, 1987], and may include contributions from shear instabilities of the alongshore current [Oltman-Shay *et al.*, 1989, Bowen

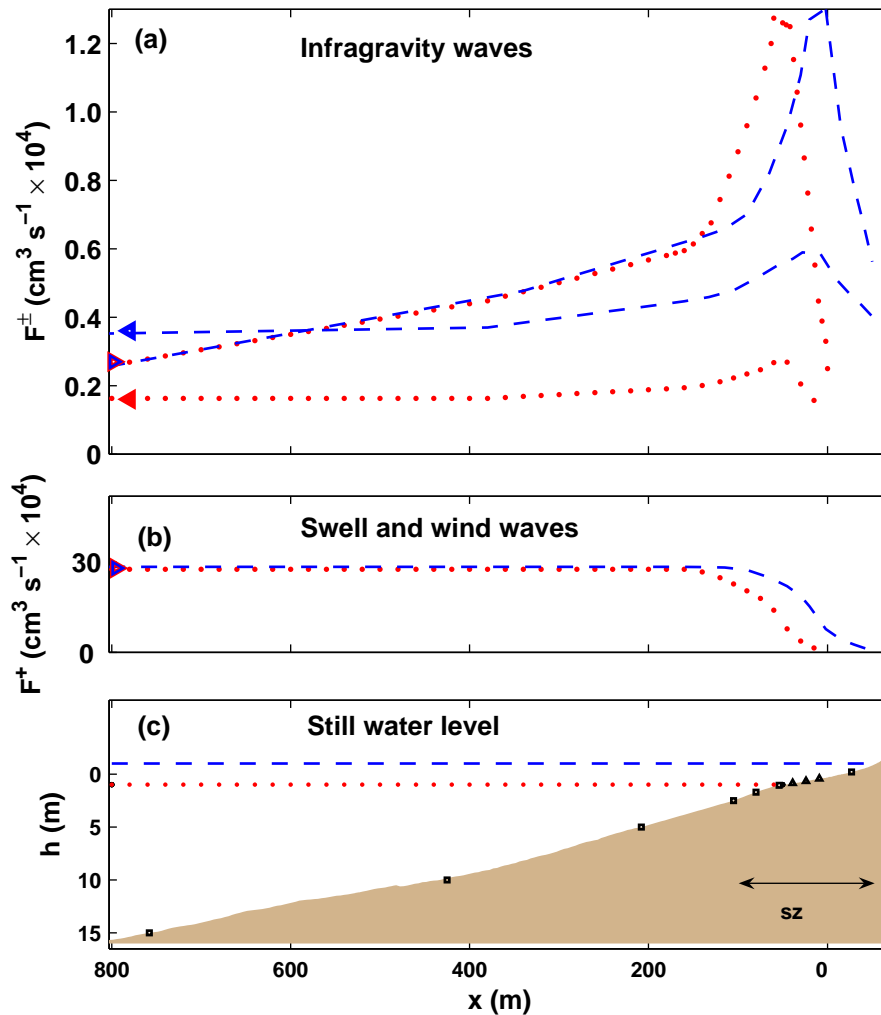


Figure 2-2: (a) Infragravity and (b) swell- and wind-wave energy flux ($\text{cm}^3 \text{s}^{-1}$) and (c) water depth (m) versus cross-shore distance (m) along the $y = 2.7$ km transect (Figure 1-3). Symbols in (c) show the locations of colocated pressure gages and current meters deployed for a 21-day period (squares) that included 4 days (triangles) of additional instrumentation in the surfzone (region labeled 'sz'). Energy fluxes are means from approximately 45 high (blue-dashed curves) and 45 low (red-dotted curves) tide 1-hr data records spanning the 21-day period. Shoreward ("upper" curves with \triangleright) and seaward ("lower" curves with \triangleleft) infragravity energy fluxes are shown in (a), whereas only shoreward swell- and wind-wave energy flux is shown in (b) because the corresponding seaward energy flux is negligible.

and Holman, 1989]. These processes were neglected here, because the tidal modulation was observed far offshore of the trapping region, and the records (20% of the total) for which shear instabilities contributed more than 30% of the total infragravity velocity variance [Lippmann *et al.*, 1999] were excluded.

The cross-shore structure of the observed infragravity energy fluxes (Figure 2-2a) suggests that the reduction in total (shoreward plus seaward) infragravity variance offshore of the surfzone (approximately $x > 100$ m in Figure 2-2) at low tide is caused by a reduction in F^- . In the surfzone, F^- originates primarily from shoreline reflection of F^+ [Guza and Thornton, 1985, Elgar *et al.*, 1994, and others]. However, reflection coefficients ($R^2 = \frac{F^-}{F^+}$) estimated from observations at the most shoreward instrument are approximately 1 regardless of the tide (not shown), suggesting the offshore tidal modulation of F^- must be caused by a surfzone modulation of F^+ . Outside the surfzone, shoreward infragravity energy flux F^+ , which contains contributions from remote sources [Elgar *et al.*, 1992, Herbers *et al.*, 1995a] and from local generation by nonlinear interactions with swell and wind waves ($0.05 > f > 0.25$ Hz) [Herbers *et al.*, 1995b], is similar at low and high tides (Figure 2-2a). Thus, the tidal modulation of infragravity variance appears to arise from a tidal modulation of the shoreward-propagating waves inside the surfzone before waves reflect from the beach (Figure 2-2a).

2.3 Analysis

To compare low- with high-tide observations, instrument locations are normalized by the width of the surfzone for each record, so that the nondimensional cross-shore coordinate x_{sz} is 0 where the mean sea-surface intersects the shoreline, and is 1 at the seaward edge of the surfzone (defined as the location where the incoming swell- and wind-wave energy flux [equation 2.1 integrated over $0.05 < f < 0.25$ Hz] drops below 85% of the flux in 15-m water depth). Cross-shore gradients $\frac{d}{dx}$ of the infragravity

energy fluxes F^\pm (equation 2.1) are calculated dimensionally using the difference between adjacent observations, and then are mapped to the normalized coordinate. Energy flux is conserved by linear shoaling waves, and nonzero $\frac{dF^\pm}{dx}$ values give the net rate of infragravity energy flux gain or loss.

The gradients of shoreward energy flux averaged over low and high tides indicate there is a net increase in F^+ in the shoaling region and the outer surfzones (curves in Figure 2-3a, $\frac{dF^+}{dx} > 0$ for $x_{sz} > 0.7$) and a net loss in the inner surfzone (Figure 2-3a, $\frac{dF^+}{dx} < 0$ for $x_{sz} < 0.7$). The inner-surfzone losses (i.e., the area under the curves for $x_{sz} < 0.7$ in Figure 2-3a) during low tide are several times larger than during high tide, reducing the amount of infragravity energy available for reflection at the shoreline, and producing the reduction in total variance (Figure 2-1a) observed offshore. Gradients in the seaward energy fluxes $\frac{dF^-}{dx}$ are small at low and high tides (not shown).

2.3.1 Nonlinear Energy Balance

In shallow water, near-resonant nonlinear interactions result in rapid energy transfers between triads of surface-gravity waves [Freilich and Guza, 1984]. The change in energy flux at frequency f consists of contributions from interactions with pairs of waves such that the sum or difference of their frequencies equals f . Using a slowly varying (i.e., WKBJ), weakly-nonlinear energy balance [Herbers and Burton, 1997] based on the inviscid Boussinesq equations [Peregrine, 1967], the net change in shoreward energy flux F^+ at frequency f is proportional to the integral of the imaginary part of the bispectrum B [Hasselmann et al., 1963, Elgar and Guza, 1985] over all frequency pairs $(f', f - f')$ with sum frequency f , such that [Norheim et al., 1998, Eq. 2.1 in flux form],

$$\frac{dF^+}{dx} = \frac{1}{h} \int \left(3\pi f \int_{-\infty}^{+\infty} \text{Im}[B(f', f - f')] df' \right) df, \quad (2.2)$$

where the outer integral is over the infragravity frequency range to match the flux calculation (equation 2.1). The dominant exchange with an infragravity frequency f occurs within the triad $(f', f - f', f)$, where both f' and $f - f'$ are in the swell- and wind-wave frequency range and have opposite signs (i.e., a difference interaction). Here, nonlinear transfers are assigned to F^+ , and the small observed changes in F^- are neglected (consistent with the large resonance-mismatch between shoreward-propagating wind waves and seaward-propagating infragravity waves [Freilich and Guza, 1984]).

Seaward of the surfzone ($x_{sz} > 1$, Figure 2-3a), the rates of infragravity energy flux gain estimated using equation 2.1 are approximately equal to the nonlinear triad energy exchange rates (equation 2.2) at both low and high tides, consistent with previous studies of random waves on a natural beach [Norheim *et al.*, 1998, Herbers *et al.*, 2000]. In the surfzone ($x_{sz} < 1$, Figure 2-3a), the rates of infragravity energy flux loss estimated using equation 2.1 also are approximately equal (although shifted seaward) to the nonlinear triad energy exchange rates (equation 2.2). In particular, the increased loss rate observed (equation 2.1) during low tide is explained well by nonlinear transfers (equation 2.2) (Figure 2-3a). On average, when integrated over the cross-shore transect, nonlinear transfers account for more than half of the net changes in infragravity energy flux at both low (net energy loss) and high (net energy gain) tides, and for more than 70% of the tidal modulation of infragravity energy flux. The nonlinear transfers do not account for all of the changes in infragravity flux because of a spatial shift in the surfzone ($x_{sz} \sim 0.5$, Figure 2-3a) that may be owing to errors in the WKBJ assumption of slow spatial variations.

Estimates of the biphasic ($\phi = \arctan \frac{\text{Im}[B]}{\text{Re}[B]}$) between infragravity and higher frequency waves are consistent with the known evolution from $\phi = -180^\circ$ in deep water (not shown) [Longuet-Higgins and Stewart, 1963] towards $\phi = 0$ with decreasing depth (Figure 2-4) [Elgar and Guza, 1985, Janssen *et al.*, 2003, Battjes *et al.*, 2004]. In water depths less than about 1 m, $\phi > 0$ and infragravity energy is lost to higher

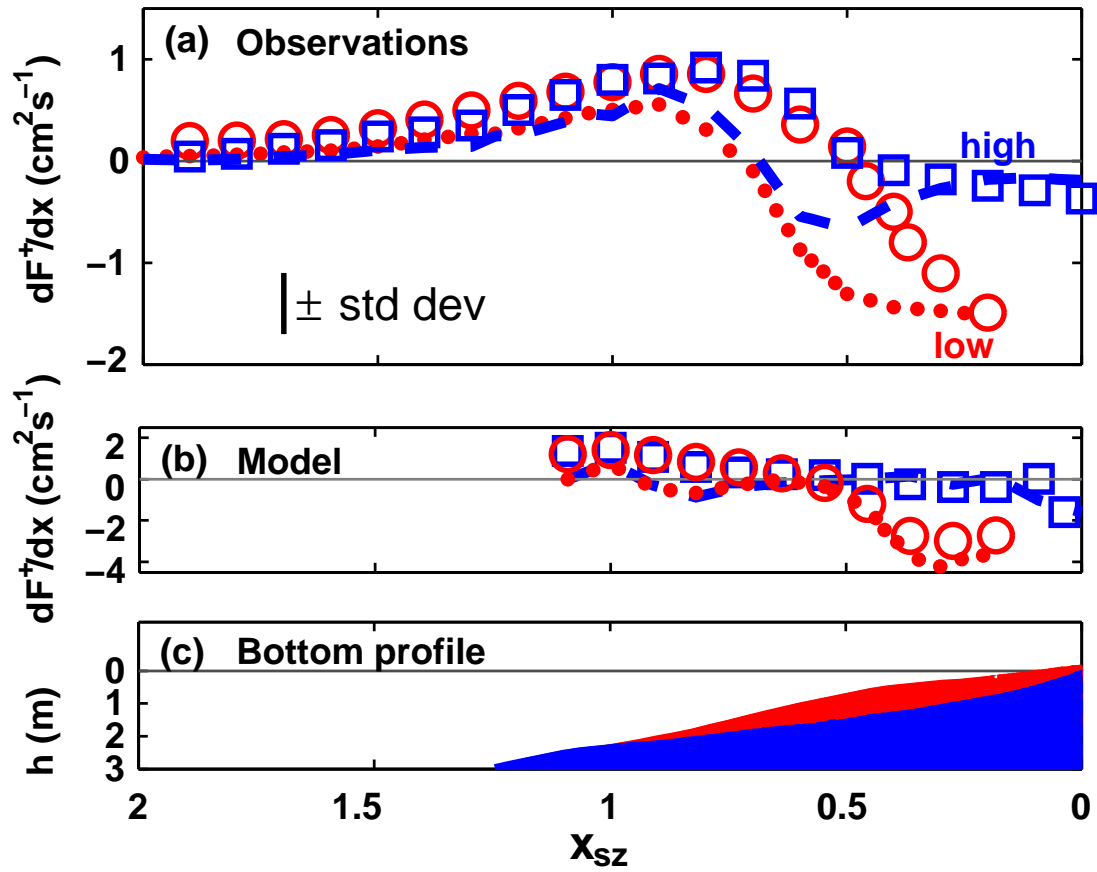


Figure 2-3: Shoreward infragravity frequency energy flux gradients $\frac{dF^+}{dx}$ from (a) observations and (b) numerical model simulations, and (c) water depth at low (red) and high (blue) tide versus normalized surfzone location (x_{sz}). The energy flux gradients $\frac{dF^+}{dx}$ are estimated from differences in the flux (F^+ , equation 2.1) between neighboring locations (red-dotted curves are low tide, blue-dashed curves are high tide) and from nonlinear transfers (equation 2.2) at each location (red circles are low tide, blue squares are high tide). The values in (a) are means of 45 1-hr records at each tide stage, with ± 1 standard deviation shown in the lower left. Tests of resolution sensitivity using a subset (8 cases each of high and low tide) of the data with 3 additional instruments in the cross-shore array confirm the validity of the gradient method. The results in (b) are from a numerically simulated case study [hence the difference in vertical scale from the averages in (a)] using the nonlinear shallow water equations at low (red dotted) and high (blue dashed) tide with identical incident waves, but different bottom profiles. Also included in (b) are estimates of the nonlinear energy transfers (equation 2.2) obtained from the simulated time series [similar to the symbols in (a)]. The cross-shore coordinate is normalized by the surfzone width, such that $x_{sz} = 0$ where the still water intersects the beach and $x_{sz} = 1$ where waves begin to break.

frequencies, however the average ϕ is not significantly different from zero (Figure 2-4).

Although tidal modulations were absent, previous studies on the North Carolina coast [*Henderson and Bowen, 2002*] identified similar cross-shore regions and rates of net infragravity gain and loss, and suggested that bottom drag may account for the observed losses, even though the drag coefficient necessary to explain the observations was an order of magnitude larger than estimates from other published studies of the nearshore region. Equation (2.2) neglects bottom drag, and instead demonstrates that nonlinear energy exchanges between infragravity waves and higher frequencies (swell and wind waves) explain most of the infragravity losses, similar to a concurrent study on the North Carolina coast [*Henderson et al., submitted, 2006*]. Although the WKBJ assumption of slow variations used to derive equation (2.2) may be violated near the shoreline on the steep North Carolina beach (where $\frac{dh}{dx} > 0.04$), for the relatively gently sloping beach here ($\frac{dh}{dx} < 0.02$ for $1.0 < h < 0.3$ m during all tidal levels), deviations owing to the WKBJ approximation are estimated to be less than 10% of the net nonlinear energy transfers at each location.

2.3.2 Numerical Model

The nonlinear transfers that reduce infragravity energy in the surfzone are simulated in a numerical model based on the fully nonlinear shallow water equations with Lax-Wendroff dissipation at bore fronts and quadratic bottom drag [*Wurjanto and Kobayashi, 1991, Raubenheimer et al., 1995*]. The model was initialized with a 1-hr time series of surface elevation (swell- and wind-wave variance = 500 cm²) calculated from bottom pressures observed in 2.5-m water depth, and run toward the shoreline over both the low- and high-tide bottom profiles (Figure 2-3c). The cross-shore structure of $\frac{dF^+}{dx}$ in the modeled time series (Figure 2-3b) is similar to that of the average of the observations (Figure 2-3a), including the enhanced energy loss at low tide.

Estimates of nonlinear transfers within the model time series (using equation 2.2) account for 80% of the net changes in infragravity energy flux (Figure 2-3b), implying

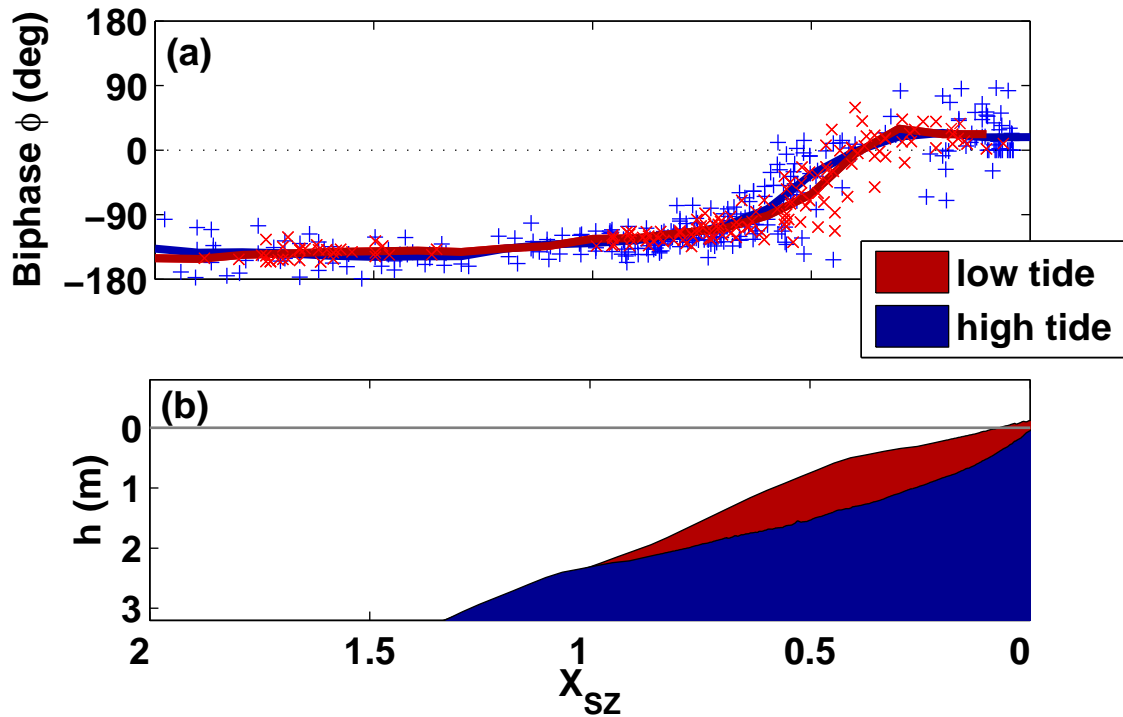


Figure 2-4: (a) Estimates of the biphase ϕ (deg) for triads of waves that include an infragravity frequency and two higher frequencies (e.g., swell and wind waves) at low (red \times) and high (blue $+$) tide and (b) bottom profile versus normalized surfzone coordinate. Solid curves in (a) are average values from the individual estimates (symbols). Only biphase values (symbols) with corresponding bicoherences significantly different from zero (95% level, [Elgar and Sebert, 1989]) are shown. The biphase evolves from the theoretical deep water limit of -180° offshore ($x_{sz} \gg 2$, not shown) to positive values in the surfzone where nonlinear losses occur (i.e., the biphase changes sign approximately where the direction of energy transfer reverses).

at most a 20% contribution from bottom friction and other loss mechanisms (assuming a perfect flux budget). The model results are insensitive to reductions in the bottom drag coefficient from the nominal [Wurjanto and Kobayashi, 1991, Raubenheimer et al., 1995] value $c_d = 0.015$. In contrast, in model tests with much larger bottom drag ($c_d = 0.05, 0.15$), bottom dissipation dominates the energy balance, and a tidal modulation is not predicted. Thus, in the numerical model, tidal modulation is caused by differences in nonlinear energy transfers over the low- and high-tide bottom profiles (Figure 2-3c) and not by differences in bottom dissipation.

2.3.3 Bottom Profile Dependence

Nonlinear transfers of infragravity energy to motions with higher frequencies were observed only in water depths less than about 1 m. The triad interactions are closer to resonance with decreasing depth and require space to transfer energy [Freilich and Guza, 1984, Herbers et al., 1995b]. Thus, although the total surfzone width does not change with the tide, the h^{-1} dependence of nonlinear triad exchanges (equation 2.2) predicts enhanced energy transfers over the convex low-tide bottom profile (compared with the concave high-tide profile), because the horizontal extent ($\int h^{-1}(x)dx$) of the shallow ($h < 1$ m) region is greater at low tide (Figure 2-3c). The tidal modulation of infragravity energy observed in 5-m water depth at eight other transects spanning 1.5 km of the coast is consistent with enhanced nonlinear energy transfers over the convex low-tide profiles (Figure 2-5).

2.4 Conclusions

Observations and numerical model simulations of ocean surface-gravity waves between 15-m water depth and the shoreline show that in the surfzone nonlinear wave-wave interactions transfer energy from low-frequency (infragravity), long waves to higher-frequency motions. The energy transfer is enhanced over the relatively flatter inner-

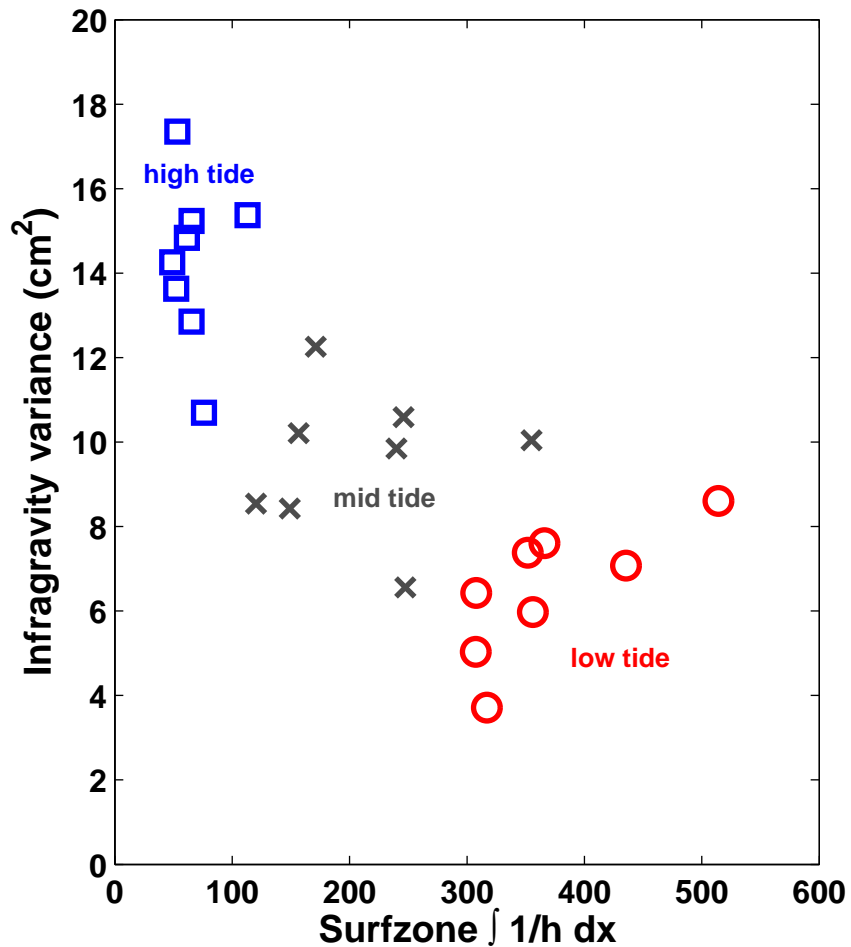


Figure 2-5: Infragravity variance observed in 5-m water depth versus the integral of h^{-1} across the surfzone at eight transects between $y = 1.2$ and $y = 2.7$ km along the coast (including the densely instrumented transect used in the cross-shore analysis). Symbols are mean values from 50 days of observations at high (blue squares), mid (gray crosses), and low (red circles) tide. The integral over the region where nonlinear losses occur ($0 < h < 1$ m) is largest at low tide because the bottom profile is flatter than at high tide.

surfzone bottom profile at low tide, explaining the tidal modulation of infragravity energy observed in bottom-pressure records on the southern California continental shelf. Similar tidal changes in beach profiles are common worldwide [*Woodroffe*, 2002, § 6.2.2], and thus tidal modulation of infragravity energy in the surfzone may affect nearshore processes and regional seismic activity in many areas.

Bibliography

- Battjes, J.A., H.J. Bakkenes, T.T. Janssen, and A.R. van Dongeren (2004), Shoaling of subharmonic gravity waves, *J. Geophys. Res.*, *109*, C02009, doi:10.1029/2003JC001863.
- Bowen, A. and R.A. Holman (1989), Shear instabilities of the mean longshore current, 1. Theory, *J. Geophys. Res.*, *94*, 18023-18030.
- Dolenc, D., B. Romanowicz, D. Stakes, P. McGill, and D. Neuhausser (2005), Observations of infragravity waves at the Monterey ocean bottom broadband station (MOBB), *Geochem. Geophys. Geosys.*, *6* (9), Q09002, doi:10.1029/2005GC000988.
- Elgar, S. and R.T. Guza (1985), Observations of bispectra of shoaling surface gravity waves, *J. Fluid Mech.*, *161*, 425-448.
- Elgar, S., T.H.C. Herbers, M. Okihiro, J. Oltman-Shay, and R.T. Guza (1992), Observations of infragravity waves, *J. Geophys. Res.*, *97*, 15573-15577.
- Elgar, S., T.H.C. Herbers, and R.T. Guza (1994), Reflection of ocean surface waves from a natural beach, *J. Phys. Oceanogr.*, *24*, 1503-1511.
- Elgar, S. and Sebert, G. (1988), Statistics of bicoherence and biphasic, *J. Geophys. Res.*, *94*, 10993-10998.
- Freilich, M.H. and R.T. Guza (1984), Nonlinear effects on shoaling surface gravity waves, *Proc. Roy. Soc. Lond.*, *A311*, 1-41.
- Guza, R.T. and E. Thornton (1985), Observations of surf beat, *J. Geophys. Res.*, *90*, 3161-3172.
- Hasselmann, K., W. Munk, and G. MacDonald (1963), Bispectra of ocean waves, in *Time Series Analysis*, edited by M. Rosenblatt, pp: 125-139, John Wiley, NY.

- Henderson, S.M. and A.J. Bowen (2002), Observations of surf beat forcing and dissipation, *J. Geophys. Res.*, *107* (C11), 3193-3203, doi:10.1029/2000JC000498.
- Henderson, S.M., R.T. Guza, S. Elgar, T.H.C. Herbers, and A.J. Bowen, Nonlinear generation and loss of infragravity wave energy, *J. Geophys. Res.*, submitted, 2006.
- Herbers, T.H.C. and M.C. Burton (1997), Nonlinear shoaling of directionally spread waves on a beach, *J. Geophys. Res.*, *102*, 21101-21114.
- Herbers, T.H.C., S. Elgar, R.T. Guza, and W. O'Reilly (1995a), Infragravity-frequency (0.005-0.05 Hz) motions on the shelf, II, Free waves, *J. Phys. Oceanogr.*, *25*, 1063-1079.
- Herbers, T.H.C., S. Elgar, and R.T. Guza (1995b), Generation and propagation of infragravity waves, *J. Geophys. Res.*, *100*, 24863-24872.
- Herbers, T.H.C., N.R. Russnogle, and S. Elgar (2000), Spectral energy balance of breaking waves within the surf zone, *J. Phys. Oceanogr.*, *30*, 2723-2737.
- Herbers, T.H.C., M. Orzech, S. Elgar, and R.T. Guza (2003), Shoaling transformation of wave frequency-directional spectra, *J. Geophys. Res.*, *108*.
- Holman, R.A. and A.J. Bowen (1982), Bars, bumps and holes: Models, *J. Geophys. Res.*, *87*, 12749-12765.
- Huntley, D., R.T. Guza, and E.B. Thornton (1981), Field observations of surf beat, 1. Progressive edge waves, *J. Geophys. Res.*, *86*, 6451-6466.
- Janssen T.T., J.A. Battjes, and A.R. van Dongeren (2003), Long waves induced by short-wave groups over a sloping bottom, *J. Geophys. Res.*, *108* (C8), 3252-3266, doi:10.1029/2002JC001515.

- Kobayashi, N. and E. Karjadi (1996), Obliquely incident irregular waves in surf and swash zones, *J. Geophys. Res.*, *101*, 6527-6542.
- Lippmann, T.C., T.H.C. Herbers, and E.B. Thornton (1999), Gravity and shear wave contributions to nearshore infragravity motions, *J. Phys. Oceanogr.*, *29*, 231-239.
- Longuet-Higgins, M. and R. Stewart (1962), Radiation stress and mass transport in gravity waves, with application to "surf beats," *J. Fluid Mech.*, *13*, 481-504.
- Munk, W., F. Snodgrass, and G. Carrier (1956), Edge waves on the continental shelf, *Science*, *123*, 127-132.
- Norheim, C.A., T.H.C. Herbers, and S. Elgar (1998), Nonlinear evolution of surface wave spectra on a beach, *J. Phys. Oceanogr.*, *28*, 1534-1551.
- Okihiro, M. and R.T. Guza (1995), Infragravity energy modulation by tides, *J. Geophys. Res.*, *100*, 16143-16148.
- Oltman-Shay, J. and R.T. Guza (1987), Infragravity edge wave observations on two California beaches, *J. Phys. Oceanogr.*, *17*, 644-663.
- Oltman-Shay, J., P. Howd, and W. Birkeimeir (1989), Shear instability of the mean longshore current, 2. Field observations, *J. Geophys. Res.*, *94*, 18031-18042.
- Peregrine, D.H. (1967), Long waves on a beach, *J. Fluid Mech.*, *27*, 815-827.
- Raubenheimer, B., R.T. Guza, S. Elgar, and N. Kobayashi (1995), Swash on a gently sloping beach, *J. Geophys. Res.*, *100*, 8751-8760.
- Rabinovich, A. and F. Stephenson (2004), Longwave measurements for the coast of British Columbia and improvements to the tsunami warning capability, *Natural Hazards*, *32*, 313-343.

- Rhie, J. and B. Romanowicz (2004), Excitation of Earth's continuous free oscillations by atmosphere-ocean-seafloor coupling, *Nature*, *431*, 552-556.
- Sheremet, A., R.T. Guza, S. Elgar, and T.H.C. Herbers (2002), Observations of nearshore infragravity waves: seaward and shoreward propagating components, *J. Geophys. Res.*, *107* (C8), 3095, doi:10.1029/2001JC000970.
- Tanimoto, T. (2005), The oceanic excitation hypothesis for the continuous oscillation of the Earth, *Geophys. J. Int.*, *160*, 276-288.
- Thomson, J., S. Elgar, B. Raubenheimer, T.H.C. Herbers, and R.T. Guza (2006), Tidal modulation of infragravity waves via nonlinear energy losses in the surf-zone, *Geophys. Res. Lett.*, *33*, L05601, doi:10.1029/2005GL025514.
- Tucker, M. (1950), Surf beats: sea waves of 1 to 5 minute period, *Proc. Roy. Soc. Lon.*, *A202*, 565-573.
- Van Dongeren, A.P., J. Van Noorloos, K. Steenhauer, J. Battjes, T. Janssen, and A. Reniers (2004), Shoaling and shoreline dissipation of subharmonic gravity waves, *Int. Conf. Coastal Eng.*, 1225-1237.
- Webb, S., X. Zhang, and W. Crawford (1991), Infragravity waves in the deep ocean, *J. Geophys. Res.*, *96*, 2723-2736.
- Woodroffe, C.D. (2002), *Coasts: form process and evolution*, Cambridge Univ. Press, New York.
- Wurjanto, A. and N. Kobayashi (1991), Numerical model for random waves on impermeable coastal structures and beaches, *Res. Rep. CACR-91-05*, Cent. for Appl. Coastal Res., Univ. of Delaware, Newark.

Chapter 3

Reflection and tunneling of ocean waves observed at a submarine canyon

Parts of this chapter were reprinted with permission from:
Thomson, J., S. Elgar, and T.H.C. Herbers (2005),
Reflection and tunneling of ocean waves observed at a submarine canyon,
Geophys. Res. Lett., **32**, L10602, doi:10.1029/2005GL022834.
Copyright 2005, *American Geophysical Union*.

Abstract

Ocean surface gravity waves with periods between 20 and 200 s were observed to reflect from a steep-walled submarine canyon. Observations of pressure and velocity on each side of the canyon were decomposed into incident waves arriving from distant sources, waves reflected by the canyon, and waves transmitted across the canyon. The observed reflection is consistent with long-wave theory, and distinguishes between cases of normal and oblique angles of incidence. As much as 60% of the energy of waves approaching the canyon normal to its axis was reflected, except for waves twice as long as the canyon width, which were transmitted across with no reflection. Although waves approaching the canyon at oblique angles cannot propagate over the canyon, total reflection was observed only at frequencies higher than 20 mHz, with lower frequency energy partially transmitted across, analogous to the quantum tunneling of a free particle through a classically impenetrable barrier.

3.1 Introduction

Surface waves with periods between 20 and 200 s (deep water wavelengths between about 500 and 50,000 m) are important to a range of geophysical processes. These infragravity motions are observed in seafloor pressure signals in deep [Webb *et al.*, 1991], coastal [Munk *et al.*, 1956, Tucker, 1950], and nearshore [Guza and Thornton, 1985, Elgar *et al.*, 1992] waters. Recent observations suggest that infragravity waves force resonant oscillations in the earth's crust [Rhie and Romanowicz, 2004], deform ice sheets [Menemenlis *et al.*, 1995], and can be used as proxies to detect tsunamis [Rabinovich and Stephenson, 2004]. Much of the infragravity energy in the ocean is generated nonlinearly by swell and wind waves in shallow water [Longuet-Higgins and Stewart, 1962, Herbers *et al.*, 1995] and reflected seaward at the shoreline [Elgar *et al.*, 1994]. Close to the shoreline, infragravity waves can contain more than 50% of the energy of the wave field [Guza and Thornton 1985], drive shallow water circulation [Kobayashi and Karjadi, 1996], and affect shoreline sediment transport and morphological evolution [Guza and Inman, 1975, Werner and Fink, 1993]. Consequently, models for nearshore processes must account for the generation, propagation, and dissipation of infragravity waves. Here, the strong effect of abrupt shallow water topography (Figure 3-1) on infragravity wave propagation is shown to be consistent with theoretical predictions [Kirby and Dalrymple, 1983], and thus can be included in models for coastal waves, currents, and morphological evolution.

3.2 Theory

The reflection and transmission of long waves ($L/h \gg 1$, where L is the wavelength and h is water depth) at a long, rectangular submarine canyon of width W are given by [Kirby and Dalrymple, 1983]

$$R^2 = \frac{\gamma}{1 + \gamma}, \quad T^2 = \frac{1}{1 + \gamma}, \quad (3.1)$$

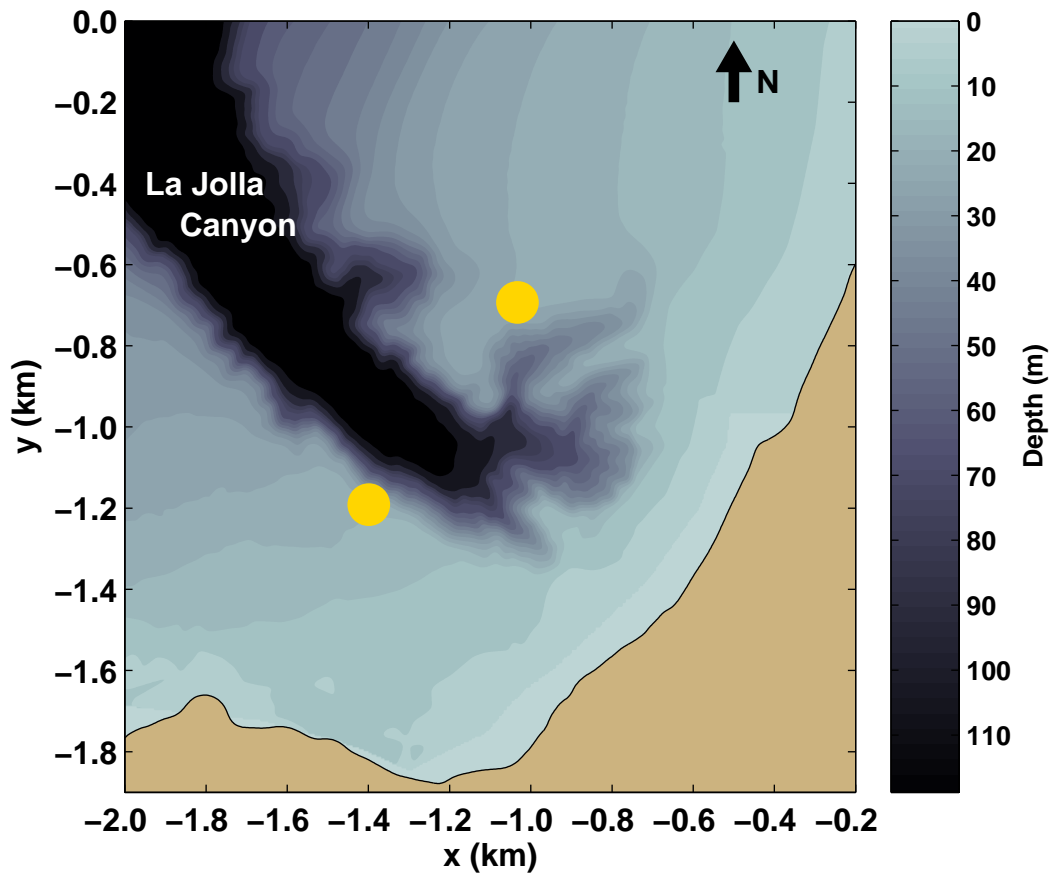


Figure 3-1: Detailed bathymetry (shaded contours) and adjacent coast (tan region) near a steep-walled submarine canyon on the Southern California coast. The La Jolla canyon (dark region) is approximately 115 m deep and 365 m wide, and the surrounding shelf is approximately 20 m deep. The circles on either side of the canyon are locations of pressure gauges and current meters mounted 1 m above the seafloor for 4 weeks during fall of 2003.

and

$$\gamma = \left(\frac{h^2 l^2 - h_c^2 l_c^2}{2hlh_c l_c} \right)^2 \sin^2(l_c W), \quad (3.2)$$

where R^2 and T^2 are the ratios of reflected and transmitted energy, respectively, to the incident energy, and energy is conserved such that $R^2 + T^2 = 1$. The cross-canyon components of the wavenumber vector in water depths within (h_c) and outside (h) the canyon are given by l_c and l , respectively. Assuming Snell's law [Mei, 1989], the along-canyon component (m) does not change as waves propagate across the canyon. The dependence of the wavenumber magnitude ($k = 2\pi/L$) on wave radian frequency (ω) and water depth (h) is given by the shallow water dispersion relation, $\omega = k\sqrt{gh}$, where g is gravitational acceleration.

When waves arrive nearly perpendicular to the axis of the canyon (i.e., normal incidence), the cross-canyon wavenumber $l_c = \sqrt{k_c^2 - m^2}$ is real (i.e., $k_c > m$), and free wave solutions exist both within and outside of the canyon. For normal incidence, the amount of reflection depends primarily on the width of the canyon relative to the wavelength (Eq. 3.2). For example, for a rectangular canyon with $h = 20$ m, $h_c = 115$ m, and $W = 365$ m (similar to La Jolla Canyon, Figure 3-1), Eqs. 3.1 and 3.2 predict that reflection increases from zero to half of the incident energy as wavelengths decrease from about 2400 (frequency of 6 mHz) to 600 m (23 mHz) (Figure 3-2a). Normally incident waves with wavelengths that are integer multiples of twice the canyon width (W) are transmitted completely across the canyon (e.g., Figure 3-2a, where $R^2 = 0$ and $T^2 = 1$ for 40 mHz waves [$L_c \approx 730$ m] normally incident to La Jolla Canyon [$W = 365$ m]). The absence of reflection is the result of a standing wave pattern between the canyon walls that is in phase with the incident waves, allowing the amplitude at the far side of the canyon to equal the amplitude at the near side of the canyon [Mei, 1989, Meyer, 1979].

In contrast, if waves approach the canyon axis obliquely, defined here as $k_c < m$, so that $l_c = \sqrt{k_c^2 - m^2}$ is imaginary, then no free wave solution exists in the deep water over the canyon, and nearly all the incident energy is reflected (Figure 3-2b). In the

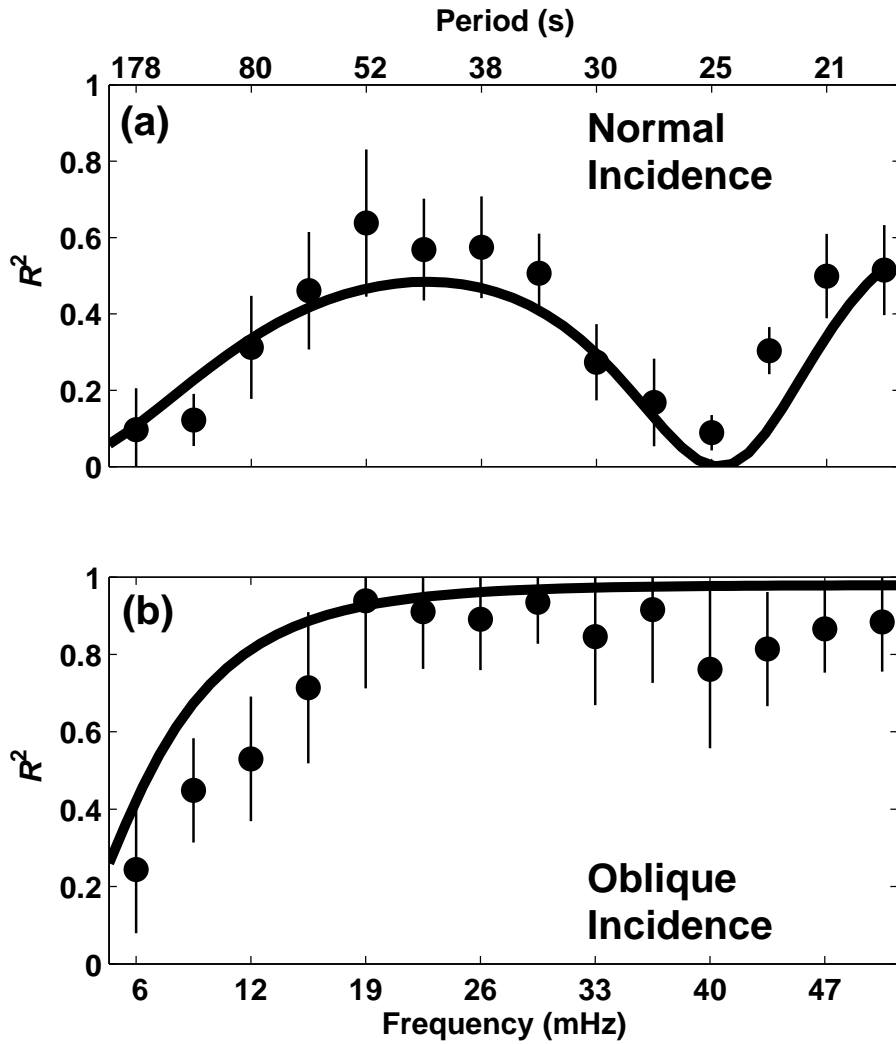


Figure 3-2: Reflection coefficients R^2 versus frequency (mHz) and period (s) for (a) normally and (b) obliquely incident waves. The curves are based on linear long-wave theory [Kirby and Dalrymple, 1983] for a rectangular approximation of the canyon cross-section with depth $h = 115$ m and width $W = 365$ m. Theory curves are similar for other rectangular approximations of the canyon profile that preserve the cross-sectional area, and also are similar over the range of angles in each category (i.e., normal and oblique). Circles are the averages of the 50 total nonlinear inverse estimates of R^2 at each frequency and vertical lines are \pm one standard deviation of the estimates. Prior to averaging over cases of normal incidence (typically about 20 cases) or cases of oblique incidence (typically about 30 cases), individual R^2 values are weighted by the narrowness of the corresponding directional spectrum, such that R^2 for narrow directional spectra are weighed more heavily than R^2 for broad spectra.

long-wave approximation, the critical angle for total reflection, $|\theta| = \arcsin(\sqrt{h/h_c})$, is independent of frequency. For the rectangular idealization of La Jolla Canyon (Figure 3-1), $|\theta| \approx 25^\circ$. However, for wavelengths (L_c) greater than about 1600 m (i.e., frequencies less than about 20 mHz in Figure 3-2b), a decaying (i.e., evanescent) wave over the finite-width canyon excites a free wave at the far side of the canyon [Mass, 1996], resulting in partial transmission of wave energy (Figure 3-3a).

The reflection and transmission of wave energy at the canyon (Figure 3-3a) is equivalent to “frustrated total internal reflection” in optics and particle tunneling in quantum mechanics [Krane, 1996, §5.7]. For example, the solution for the quantum tunneling of a free particle with energy E through a potential energy barrier of amplitude U and width W (Figure 3-3b) can be written by replacing Eq. 3.2 with

$$\gamma = \frac{U^2}{4E(E-U)} \sin^2\left(\frac{2\pi W}{\lambda}\right), \quad (3.3)$$

where λ is the de Broglie wavelength of the particle. The resulting reflection and transmission coefficients (Eq. 3.1) describe the probability of observing the particle on either side of the barrier. To the wavelike properties (e.g., λ) of the quantum particle, the barrier acts as a one-dimensional finite-width change in refractive medium [Krane, 1996]. When the energy of the particle is greater than the energy of the barrier ($E > U$), the particle may propagate across the barrier, similar to a wave of normal incidence ($k_c > m$) propagating across the canyon. In contrast, when $E < U$, the barrier is classically impenetrable, similar to a wave approaching the canyon at an oblique ($k_c < m$) angle. Although a particle with $E < U$ cannot be observed within the barrier region, there is a nonzero probability of observing the particle across the barrier when the de Broglie wavelength (λ) is large compared to the width of the barrier (analogous to the partial transmission of obliquely incident waves across a finite-width submarine canyon).

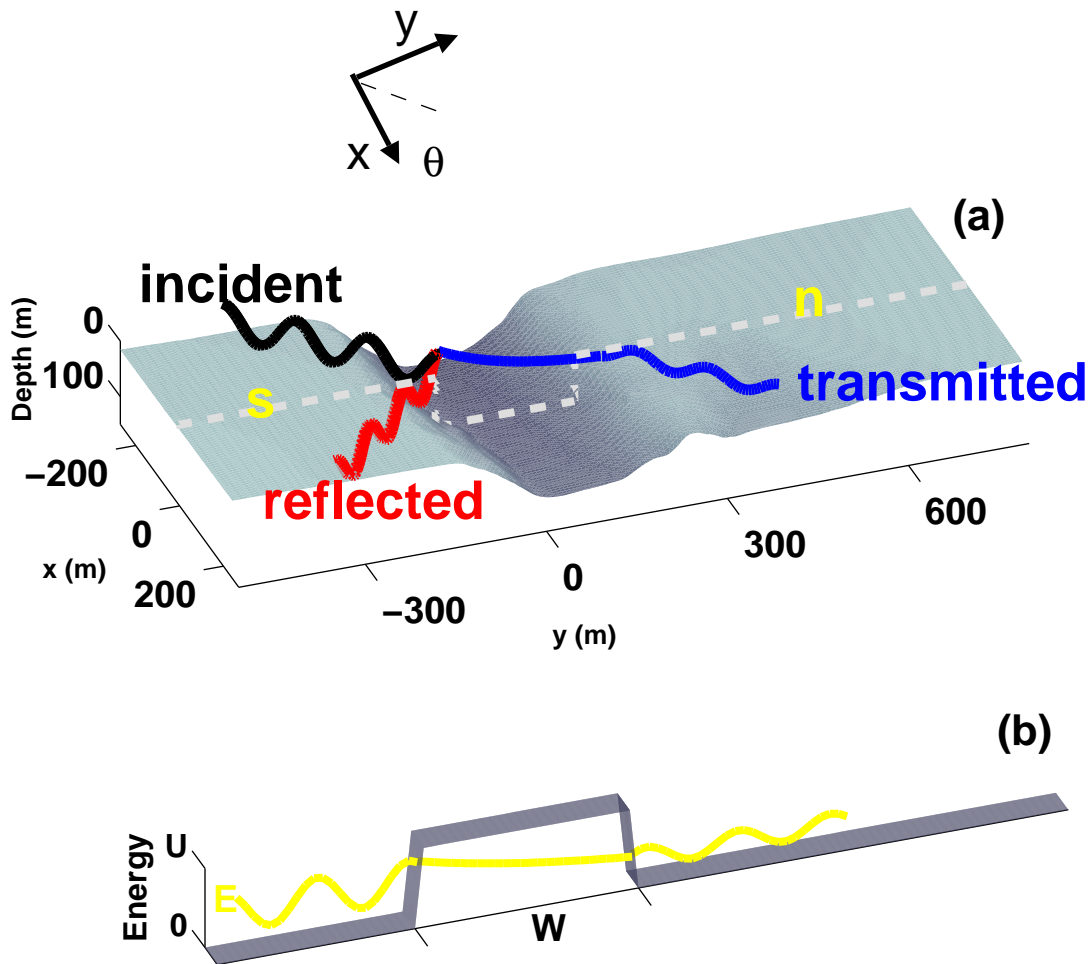


Figure 3-3: Schematic diagrams showing partial reflection of an oblique wave by a submarine canyon and quantum tunneling across an energy barrier. (a) Partial reflection of an obliquely incident wave (black curve) over the measured canyon bathymetry (shaded surface). A decaying wave over the canyon excites a transmitted wave (blue curve) on the far side, even though there is no propagation within the canyon. The transmitted wave (blue curve) preserves the angle θ relative to the cross-canyon coordinate y , while the reflected wave (red curve) reverses the angle. Depth is measured in meters below mean sea level, and a rectangular idealization of the canyon cross-section with $h=20$ m, $h_c=115$ m, and $W=365$ m is shown as a grey dashed line between the south (s) and north (n) instrument sites. (b) Quantum tunneling of a free particle (yellow curve) with energy E through a finite width W region of potential energy U , where $E < U$ and the region is classically forbidden. The scale of the decaying solution in the forbidden region is set by the de Broglie wavelength of the particle.

3.3 Field Observations

To test Eqs. 3.1 and 3.2 in the ocean, measurements of surface-wave-induced pressure and velocity were made with colocated sensors deployed in 20-m water depth (tide range about 1 m) approximately 200 m north and 100 m south of La Jolla Submarine Canyon, near San Diego, California (Figure 1) for 4 weeks during the fall of 2003. Infragravity wave (5 to 50 mHz) significant heights (4 times the sea-surface elevation standard deviation) ranged from 0.01 to 0.20 m. Reflection coefficients were estimated from the 50 (of 327 total) two-hr long time series (sampled at 1000 mHz) with infragravity significant heights greater than 0.05 m at both sides of the canyon. For records with significant heights below 0.05 m, estimates of reflection coefficients may be contaminated by noise in the pressure and velocity measurements.

In contrast to the unidirectional waves used in a laboratory investigation of Eqs. 3.1 and 3.2 [Kirby and Dalrymple, 1983], ocean waves can have broad directional distributions that differ on each side of the canyon. The random wave fields on the north (n) and south (s) sides of the canyon consist of incident, reflected, and transmitted (from the other side of the canyon) waves (Figure 3-3a), such that the surface elevations η_s and η_n can be written as integrals over wave components at each frequency and direction, given by

$$\eta_s = \int_{\omega} \int_{\theta=-\frac{\pi}{2}}^{\frac{\pi}{2}} d_s \left(e^{i(mx+ly-\omega t)} + R_s e^{i(mx-ly-\omega t+\psi_s)} \right) + d_n \left(T_n e^{i(mx-ly-\omega t)} \right), \quad (3.4)$$

$$\eta_n = \int_{\omega} \int_{\theta=-\frac{\pi}{2}}^{\frac{\pi}{2}} d_n \left(e^{i(mx-ly-\omega t)} + R_n e^{i(mx+ly-\omega t+\psi_n)} \right) + d_s \left(T_s e^{i(mx+ly-\omega t)} \right), \quad (3.5)$$

where d_s and d_n are the complex-valued differential amplitudes of the incident wave components at radian frequency ω and direction θ relative to the local cross-canyon coordinate y . The variables R_s , R_n , T_s , and T_n are reflection and transmission coefficients, ψ_s and ψ_n are the phase shifts of the reflected waves relative to the incident waves, x is the local along-canyon coordinate, and t is time. Reflection is assumed

to be specular, and thus the sign of the cross-canyon wavenumber ($l = k \cos \theta$) is reversed upon reflection, while the sign of the along-canyon wavenumber ($m = k \sin \theta$) is preserved (Figure 3-3a). In this two-quadrant ($-\frac{\pi}{2} < \theta < \frac{\pi}{2}$) system, the direction of y propagation is given explicitly by the sign of the exponent in $e^{\pm ly}$ because l is always positive.

3.4 Methods

In contrast to methods used to estimate the amount of reflection from impermeable structures [Dickson *et al.*, 1995], estimation of the reflection of a canyon must also account for transmission. Here, inverse techniques [Coleman and Li, 1996] are used to determine the reflection (R_s, R_n) and transmission (T_s, T_n) coefficients, as well as the incident directional spectra (D_s, D_n) and reflected phases (ψ_s, ψ_n) of the wave fields on the south (s) and north (n) sides of the canyon that are most consistent with observations of pressure and velocity.

The cross-canyon velocity v , along-canyon velocity u , and pressure p fields induced by surface waves (Eqs. 3.4 and 3.5) can be determined from a linear, hydrostatic momentum balance (appropriate for infragravity waves in 20-m water depth) given by

$$\frac{\partial v}{\partial t} = -g \frac{\partial \eta}{\partial y}, \quad \frac{\partial u}{\partial t} = -g \frac{\partial \eta}{\partial x}, \quad p = \rho g \eta, \quad (3.6)$$

where g is gravitational acceleration and ρ is density.

Substituting η_s and η_n into the momentum balance (Eq. 3.6), using the Fourier transformed result, and applying the identities $2i \sin(i\alpha) = e^{-\alpha} - e^{\alpha}$ and $2 \cos(i\alpha) = e^{\alpha} + e^{-\alpha}$ yields the following expressions for the frequency cross-spectra of the collocated pressure and velocity time series south (s) of the canyon

$$\langle p_s(\omega) \cdot u_s^*(\omega) \rangle = \rho g \kappa \int_{\theta} \sin \theta \left[D_n T_n^2 + D_s \left(1 + R_s^2 + 2R_s \cos \psi_s \right) \right] d\theta, \quad (3.7)$$

$$\langle p_s(\omega) \cdot v_s^*(\omega) \rangle = \rho g \kappa \int_{\theta} \cos \theta \left[-D_n T_n^2 + D_s \left(1 - R_s^2 + \mathbf{i} 2 R_s \sin \psi_s \right) \right] d\theta, \quad (3.8)$$

$$\langle u_s(\omega) \cdot v_s^*(\omega) \rangle = \kappa^2 \int_{\theta} \sin \theta \cos \theta \left[-D_n T_n^2 + D_s \left(1 - R_s^2 + \mathbf{i} 2 R_s \sin \psi_s \right) \right] d\theta, \quad (3.9)$$

where $\kappa = \frac{gk}{\omega}$, \star is the complex conjugate, and $\langle \rangle$ is the expected value. Similarly, the auto-spectra are

$$\langle p_s(\omega) \cdot p_s^*(\omega) \rangle = (\rho g)^2 \int_{\theta} \left[D_n T_n^2 + D_s \left(1 + R_s^2 + 2 R_s \cos \psi_s \right) \right] d\theta, \quad (3.10)$$

$$\langle u_s(\omega) \cdot u_s^*(\omega) \rangle = \kappa^2 \int_{\theta} \sin^2 \theta \left[D_n T_n^2 + D_s \left(1 + R_s^2 + 2 R_s \cos \psi_s \right) \right] d\theta, \quad (3.11)$$

$$\langle v_s(\omega) \cdot v_s^*(\omega) \rangle = \kappa^2 \int_{\theta} \cos^2 \theta \left[D_n T_n^2 + D_s \left(1 + R_s^2 - 2 R_s \sin \psi_s \right) \right] d\theta, \quad (3.12)$$

The incident wave directional spectra D_s and D_n are defined as

$$D_s(\omega, \theta) = \frac{\langle d_s \cdot d_s^* \rangle}{d\omega d\theta}, \quad (3.13)$$

$$D_n(\omega, \theta) = \frac{\langle d_n \cdot d_n^* \rangle}{d\omega d\theta}. \quad (3.14)$$

The incident wave fields on the north and south sides of the canyon are independent of each other, and thus $\langle d_s \cdot d_n^* \rangle = \langle d_n \cdot d_s^* \rangle = 0$.

Expressions for cross- and auto-spectra at the north side of the canyon are obtained by exchanging all subscripts ($s \leftrightarrow n$) in the expressions above (Eqs. 3.7-3.12) and changing the sign of the integrand in Eqs. 3.8 and 3.9.

The real-valued terms describe the progressive wave field, and the imaginary (\mathbf{i}) terms (i.e., the quadrature in the cross-spectra $\langle p \cdot v^* \rangle$ and $\langle u \cdot v^* \rangle$) describe the partial standing wave patterns owing to sums of incident and reflected waves. In practice, the expressions for cross- and auto-spectra apply only to observations near the canyon walls, because over large distances (i.e., many wavelengths) standing wave patterns are obscured within a finite-width frequency band.

For computational efficiency, the incident directional spectra (Eqs. 3.13 and 3.14)

at each frequency band are modeled as [Donelan *et al.*, 1985]

$$D_s(\theta) = M_s \cos^{2S_s} \left(\frac{\theta - \Theta_s}{2} \right), \quad (3.15)$$

$$D_n(\theta) = M_n \cos^{2S_n} \left(\frac{\theta - \Theta_n}{2} \right), \quad (3.16)$$

where Θ_s and Θ_n are the centroidal directions, S_s and S_n describe the spread in direction about the centroid, and M_s and M_n are the spectral peak values. The results are insensitive to the specific unimodal shape used for the incident directional spectra. The centroidal directions Θ_s and Θ_n were used to separate the data sets (at each frequency band) into normally ($|\Theta| < 20^\circ$) and obliquely ($|\Theta| > 30^\circ$) incident waves. Assuming directionally narrow spectra, the reflection (R_s, R_n) and transmission (T_s, T_n) coefficients are assumed to be independent of direction at each frequency.

The phase shifts ψ_s and ψ_n of the reflected waves relative to the incident waves were allowed to vary over each directional spectrum by assuming

$$\psi_s(\theta) = 2\Delta y_s k \cos \theta, \quad (3.17)$$

$$\psi_n(\theta) = 2\Delta y_n k \cos \theta, \quad (3.18)$$

where Δy_s and Δy_n are the (unknown) distances between the reflector and the instrument locations (i.e., ψ is the phase change associated with propagating toward and back from the reflector).

Assuming energy is conserved (i.e., $R_s^2 + T_s^2 = 1$, $R_n^2 + T_n^2 = 1$), the inverse method finds the north (n) and south (s) values of Θ, S, M, R , and Δy that are most consistent with the cross- and auto-spectra of the observed time series by minimizing a normalized root-mean-square error [Dickson *et al.*, 1995]

$$\epsilon = \sqrt{\frac{\sum(\text{obs} - \text{derived}) \cdot (\text{obs} - \text{derived})^*}{\sum(\text{obs})(\text{obs})^*}}, \quad (3.19)$$

where Σ is the sum over the six auto- and cross-spectral values from the south side (Eqs. 3.7-3.12) and the six spectral values from the north side. Applying recent improvements to Newton's method [Coleman and Li, 1996], the inverse algorithm begins with an initial guess for each unknown, and solves a locally linearized version of the equations for the cross- and auto-spectra to find the small change in each unknown that produces the greatest reduction in ϵ (i.e., the method iterates down-slope in ϵ until the minimum is found). Initial guesses for Θ , S , and M are provided by estimates of directional moments of the wave field based on the measured pressure and velocities [Kuik *et al.*, 1988], and the initial guesses for R are based on long-wave theory [Kirby and Dalrymple, 1983]. The results (Figure 3-2) are not sensitive to the initial values, and the same inverse solutions are obtained with random initial guesses (although computational time is increased).

3.5 Results

For waves normally incident to the canyon axis, reflection coefficients estimated with the inverse method are consistent with long-wave theory (Figure 3-2a), including the nearly complete transmission of waves with wavelength twice the canyon width ($W = 365$ m, $L_c \approx 730$ m, frequency = 40 mHz). When unidirectional waves are normally incident on each side of the canyon (i.e., symmetric normal incidence), a forward calculation can be used to estimate reflection, and the few cases that satisfied these criteria also are consistent with long-wave theory (not shown). Inverse estimates of reflection coefficients for waves obliquely incident to the canyon axis also are consistent with theory, including the nearly complete reflection of waves with frequencies above about 20 mHz, and the tunneling that results in reduced reflection of lower frequency waves (Figure 3-2b).

The observed reflection of obliquely incident waves is somewhat less than theoretical predictions (Figure 3-2b), possibly because the neglected non-uniformity of the

La Jolla Canyon profile (Figure 3-1) becomes increasingly important as the incidence angle increases. The reduction in the sharpness of the canyon results in reduced reflection, and also may contribute to the scatter within the reflection coefficients at each frequency band (Figure 3-2). Directionally spread wave fields that simultaneously contain energy at both normal and oblique angles likely increase the scatter. To reduce this effect, the spreading parameters (S_s , S_n) were used to weight individual estimates of R^2 by

$$R_{\text{avg}}^2 = \frac{\sum S_s R_s^2 + S_n R_n^2}{\sum S_s + S_n} \quad (3.20)$$

to calculate an average value R_{avg}^2 at each frequency from the collection of data runs (e.g., the symbols in Figure 3-2).

Statistical fluctuations in the cross-spectra of finite-length data records may produce additional scatter in the results [Wunsch, 1996], and the residual errors (Eq. 3.19) approximately follow the expected χ^2 distribution of such fluctuations. The percent of observed variance captured by the inverse method (defined as $100 \times [1 - \epsilon^2]$) is 90% when averaged over all infragravity frequency bands for all 50 data sets.

Estimates of the phase differences ψ_s and ψ_n between incident and reflected waves are consistent with the travel time required for a wave to propagate to the reflector and back (Figure 3-4), providing a consistency check on the inverse solutions. The small deviations from theoretical phase shifts may be owing to errors in approximating the sloped canyon walls as vertical. Further investigation of the reflected wave phase lags could be used to investigate the effect of a spatially distributed reflector (e.g., reflection by sloping, irregularly shaped walls). Alternatively, the inverse method could be restructured as an over-determined set of equations by specifying ψ_s and ψ_n as known from measurements of Δy_s and Δy_n (i.e., assuming Eqs. 3.17 and 3.18 are valid), but at the expense of being able to verify the solutions.

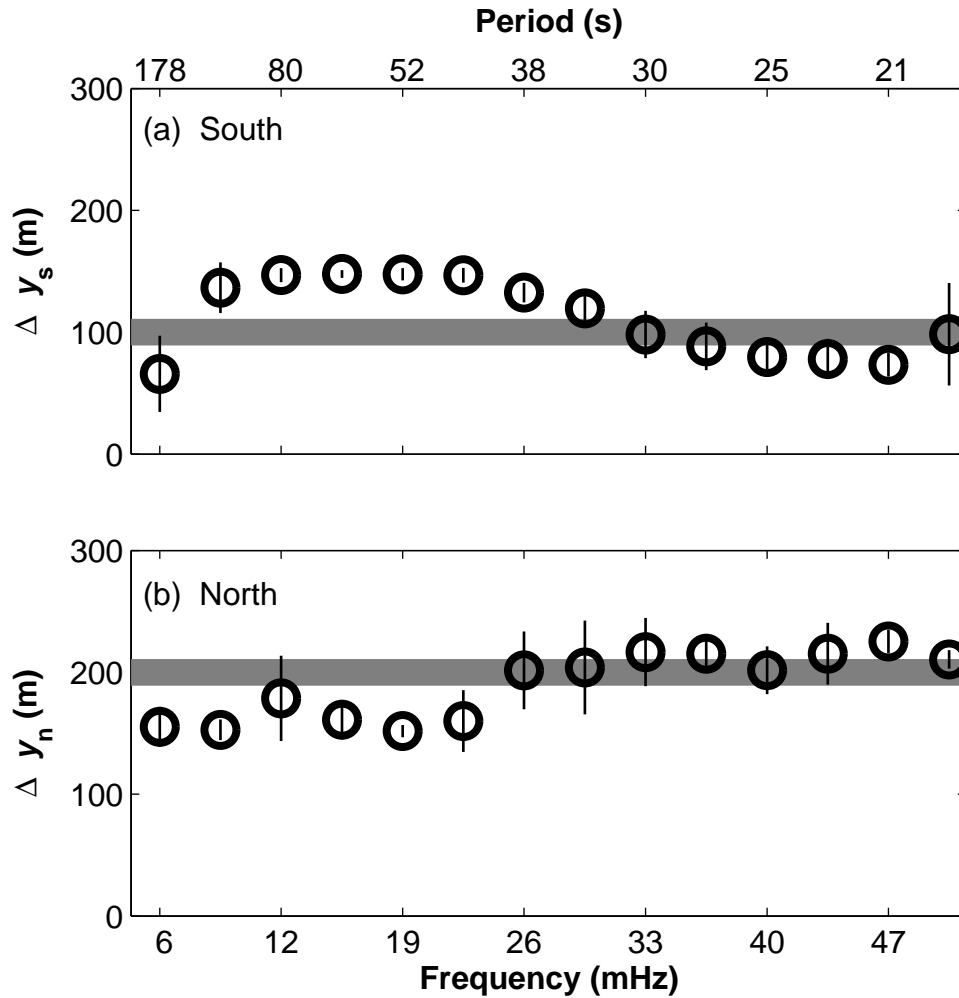


Figure 3-4: Distance (m) between the reflector and the instrument location versus frequency (mHz) and period (s) at the (a) south and (b) north sides of the canyon. Symbols are estimates from the nonlinear inverse method and solid lines are the measured distances from the steepest portion of each canyon slope to the instrument site at that side. Instrument locations were determined within ± 10 m (the width of the solid lines) with differential GPS. The theory assumes that waves propagate from the instrument site to a vertical-canyon-wall reflector along a line of constant y and back, neglecting possible phase shifts at the sloped walls. Vertical lines are \pm one standard deviation of the estimates.

3.6 Conclusions

During the 4-week observational period, on average more than half the incident infragravity wave energy was reflected by La Jolla submarine canyon. Although low frequency (less than about 20 mHz) waves arriving at angles oblique to the canyon axis cannot propagate within the canyon, a tunneling phenomenon predicts that reflection is only partial (i.e., some energy is transmitted across the canyon), consistent with the observations. These results suggest that reflection of directionally spread waves by complex shallow water bathymetry should be included in models of nearshore processes and considered as a potential shore protection method.

Bibliography

- Coleman, T. and Y. Li (1996), An interior, trust region approach for nonlinear minimization subject to bounds, *SIAM J. Optimization*, 6, 418-445.
- Dickson, W., T.H.C. Herbers, and E. Thornton (1995), Wave reflection from break-water, *J. of Water., Port, Coast., Ocean Eng.* 121, 262-268.
- Donelan, M., J. Hamilton, and W. Hui (1985), Directional spectra of wind-generated waves, *Phil. Trans. Roy. Soc. Lon.*, A315, 509-562.
- Elgar, S., T.H.C. Herbers, M. Okihiro, J. Oltman-Shay, and R. Guza (1992), Observations of infragravity waves, *J. Geophys. Res.*, 97, 15573-15577.
- Elgar, S., T.H.C. Herbers, and R.T. Guza (1994), Reflection of ocean surface waves from a natural beach, *J. Phys. Oceanogr.*, 24, 1503-1511.
- Guza, R.T. and D. Inman (1975), Edge waves and beach cusps, *J. Geophys. Res.*, 80, 2997-3012.
- Guza, R.T. and E. Thornton (1985), Observations of surf beat, *J. Geophys. Res.*, 90, 3161-3172.
- Herbers, T.H.C., S. Elgar, and R. Guza (1995), Generation and propagation of infragravity waves, *J. Geophys. Res.*, 100, 24863-24872.
- Kirby, J. and R. Dalrymple (1983), Propagation of obliquely incident water waves over a trench, *J. Fluid Mech.*, 133, 47-63.
- Kobayashi, N. and E. Karjadi (1996), Obliquely incident irregular waves in surf and swash zones, *J. Geophys. Res.*, 101, 6527-6542.
- Krane, K. (1996), *Modern Physics*, 2nd ed., John Wiley & Sons, New York.

- Kuik, A., G. Van Vledder, and L. Holthuijsen (1988), A method for the routine analysis of pitch-and-roll buoy wave data, *J. Phys. Oceanogr.* *18*, 1020-1034.
- Longuet-Higgins, M. and R. Stewart (1962), Radiation stress and mass transport in gravity waves, with application to “surf beats,” *J. Fluid Mech.*, *13*, 481-504.
- Maas, L.R.M. (1996), Topographic filtering and reflectionless transmission of long waves, *J. Phys. Oceanogr.*, *27*, 195-202.
- Mei, C.C. (1989), *The Applied Dynamics of Ocean Surface Waves*, World Scientific, New Jersey.
- Menemenlis, D., D. Farmer, and P. Czipott (1995), A note on infragravity waves in the Arctic ocean, *J. Geophys. Res.*, *100*, 7089-7094.
- Meyer, R.E. (1979), Surface wave reflection by underwater ridges, *J. Phys. Oceanogr.*, *9*, 150-157.
- Munk, W., F. Snodgrass, and G. Carrier (1956), Edge waves on the continental shelf, *Science*, *123*, 127-132.
- Rabinovich, A. and F. Stephenson (2004), Longwave measurements for the coast of British Columbia and improvements to the tsunami warning capability, *Natural Hazards*, *32*, 313-343.
- Rhie, J. and B. Romanowicz (2004), Excitation of Earth’s continuous free oscillations by atmosphere-ocean-seafloor coupling, *Nature*, *431*, 552-556.
- Thomson, J., S. Elgar, and T.H.C. Herbers (2005), Reflection and tunneling of ocean waves observed at a submarine canyon, *Geophys. Res. Lett.*, *32*, L10602, doi:10.1029/2005GL022834.
- Tucker, M. (1950), Surf beats: sea waves of 1 to 5 minute period, *Proc. Roy. Soc. Lon.*, *A202*, 565-573.

Webb, S., X. Zhang, and W. Crawford (1991), Infragravity waves in the deep ocean, *J. Geophys. Res.*, *96*, 2723-2736.

Werner, B. and T. Fink (1993), Beach cusps as self-organized patterns, *Science*, *260*, 968-971.

Wunsch, C. (1996), *The Ocean Circulation Inverse Problem*, Cambridge University Press, Cambridge.

Chapter 4

Conclusions and Regional Description

The primary result of this thesis research is an improved understanding of the effects of bottom topography on the propagation of infragravity waves. Depending on the bottom profile, in shallow water ($h < 3$ m) nonlinear interactions with swell and wind waves result in net energy transfer to or from infragravity waves [Thomson *et al.*, 2006]. In deeper water ($h > 3$ m), infragravity waves are partially reflected from, and partially transmitted across, a steep-walled canyon, consistent with linear long-wave theory [Thomson *et al.*, 2005]. In addition, the extensive field observations can be used to investigate the regional propagation of infragravity waves. In particular, the results can be combined with refraction models to simulate the propagation of infragravity waves over complex shallow water bathymetry.

4.1 Shoaling and Unshoaling

Studies on several beaches have found that infragravity motions are predominantly cross-shore oriented [Guza and Thornton, 1985, Sheremet *et al.*, 2002, Reniers *et al.*, 2006], and thus cross-shore approximations, as in Chapter 2, are common to many in-

fragravity analyses. The NCEX observations are consistent with this approximation, because, on average, alongshore motions contributed only 20% of the total infragravity velocity variance. In addition, at the nearby Torrey Pines State Beach ($y = 3.0$ km, Figure 1-3), alongshore propagating edge waves detected in shallow ($h < 3$ m) water contained only 15% of the total infragravity pressure variance [Oltman-Shay and Guza, 1987]. However, at offshore locations ($h > 5$ m, $|x| > 500$ m, Figure 1-3), NCEX observations of infragravity velocities were closer to isotropic (alongshore motions were 40%, on average, of the total velocity variance), consistent with previous observations of cross-shore dominated wave fields that became directionally broader during seaward refraction [Herbers *et al.*, 1995b].

Similar to previous results, NCEX observations of total infragravity energy across the shelf (Figure 4-1) are consistent with freely propagating waves that shoal and unshoal within the theoretical limits of $h^{-1/2}$ for cross-shore propagating waves [Elgar *et al.*, 1992, Figure 3] and h^{-1} for isotropic edge waves [Herbers *et al.*, 1995a, Figure 7]. Contributions from forced, or group bound, waves that shoal proportional to a theoretical maximum h^{-5} [Longuet-Higgins and Stewart, 1962] are small everywhere except the surfzone. Seaward propagating free waves are a significant portion of the total infragravity energy (e.g., Figure 2-2), and unshoal during refraction over the bathymetry.

4.2 Refraction and Canyon Reflections

The propagation of swell outside the surfzone is modeled accurately by the refraction of energy-flux conserving rays [Munk and Traylor, 1947, O'Reilly and Guza, 1993; and many others]. Here, a refraction model is presented that describes the seaward radiation of infragravity waves and accounts for partial reflections and transmissions at the Scripps and La Jolla canyons. The model is initialized with observations in 2.5 m depth (nominally outside the surfzone), assuming half the variance is radiated

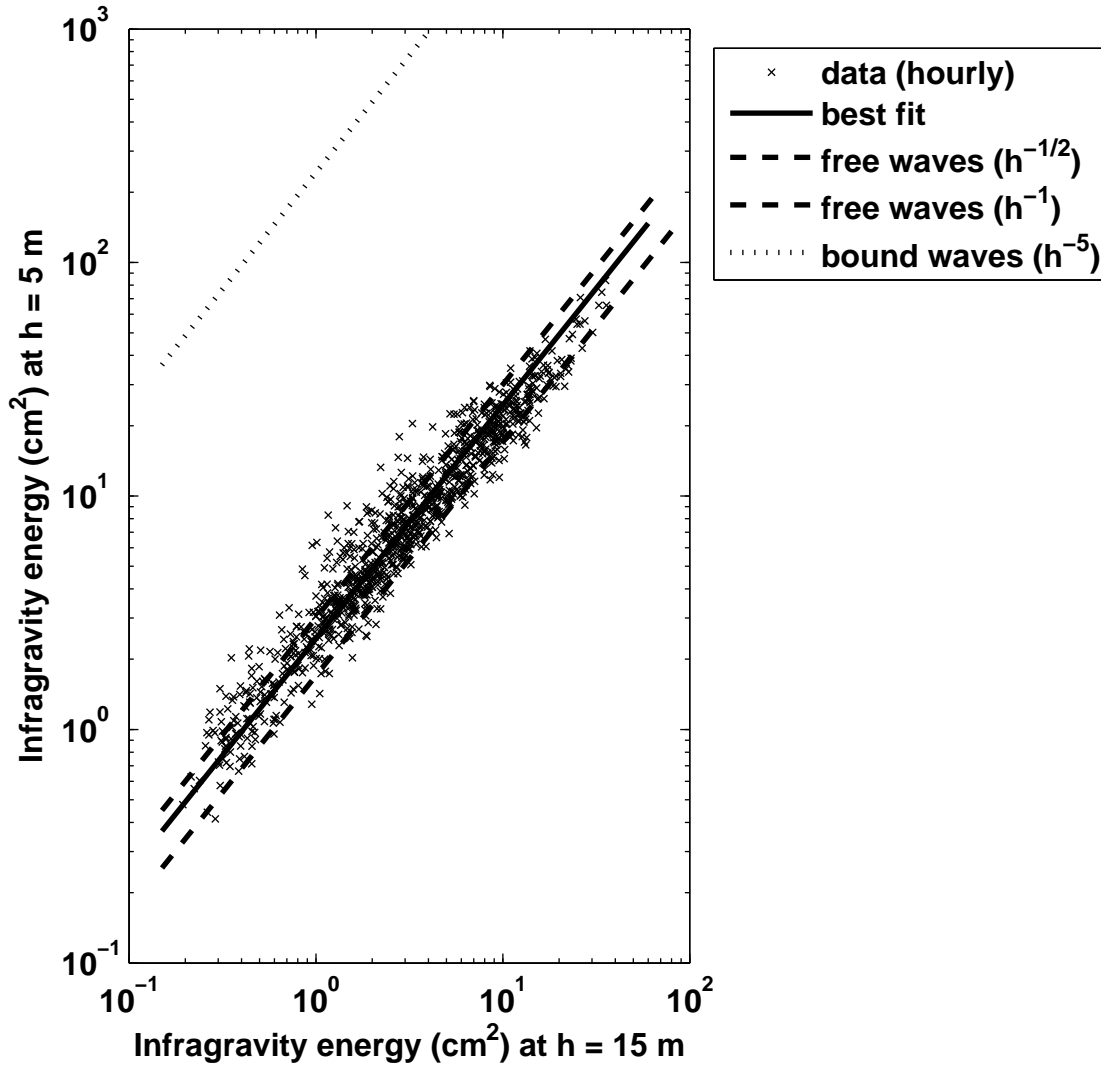


Figure 4-1: Infragravity energy (cm^2) observed at $h = 15$ m versus infragravity energy (cm^2) observed at $h = 5$ m along the northern transect ($y = 2.7$ km, Figure 1-3). The least squares linear fit (solid line, slope = 2.4, correlation = 0.95) to the hourly data (symbols) is between the theoretical $h^{-1/2}$ shoaling of cross-shore propagating free waves (lower dashed line, slope = $(5/15)^{-1/2} = 1.7$) and the theoretical h^{-1} shoaling of isotropic free edge waves (upper dashed line, slope = $(5/15)^{-1} = 3$). The observations are far from the theoretical h^{-5} shoaling of cross-shore propagating forced waves (dotted line, slope = $(5/15)^{-5} = 243$). Some spread is expected owing to tidal fluctuations (1 m), which change ratios of instrument depths slightly (but not the absolute difference in depth), such that $\left(\frac{5\pm 1}{15\pm 1}\right)^{-1/2} = 1.7 \pm 0.1$ and $\left(\frac{5\pm 1}{15\pm 1}\right)^{-1} = 3.0 \pm 0.2$.

seaward (e.g., reflection coefficient $R^2 = 1$). Subsequent reflections of energy that returns to the shoreline (along refractively trapped rays) are neglected.

Rays are traced [original code by M. Orzech, Naval Postgraduate School] using

$$x_{n+1} = x_n + ds \cos(\theta_n) \quad \text{and} \quad y_{n+1} = y_n + ds \sin(\theta_n) \quad (4.1)$$

where x and y refer to the NCEX grid (Figure 1-3), n is the integer number of ray segments along a ray path, ds is the length (5 m) of a ray segment, and the angle θ is determined by [Mei, 1989, §3.2]

$$\theta_{n+1} = \theta_n + \frac{ds}{\sqrt{gh}} \left(\sin(\theta_n) \frac{\partial \sqrt{gh}}{\partial x} - \cos(\theta_n) \frac{\partial \sqrt{gh}}{\partial y} \right), \quad (4.2)$$

using the local depth $h = h(x_n, y_n)$. Initial angles, θ_0 , are obtained from the observations or are prescribed. The partial reflections and transmissions are predicted by Eqs. 3.1 and 3.2, using rectangular approximations of the canyon cross-sections. Energy flux is conserved along each ray by shoaling and unshoaling proportional to $h^{-1/2}$. Energy flux also is conserved at each canyon where incident rays are split into reflected (at specular angles) and transmitted (angle conserved across the canyon) portions that continue to refract until returning to the surfzone (re-reflections at the shoreline are neglected) or reaching the deep water beyond the shelf. For example, ray paths of 50 s period infragravity waves propagating seaward from 2.5 m depth at an initial angle $\theta_0 = -20^\circ$ from shore normal are partially reflected by Scripps canyon (Figure 4-2), reducing the amount of wave energy that propagates southward along the shelf and refracts back to the shoreline.

To study the regional distribution of infragravity waves, ray paths are calculated for all possible frequencies (0.0068 Hz resolution) and initial angles (5° resolution) from the 2.5 m isobath. Each ray is assigned an initial relative energy flux F and direction θ_0 based on observations in 2.5 m depth, using the unimodal directional spectrum given by Eqs. 3.15 and 3.16, and interpolated to evenly spaced (50 m)

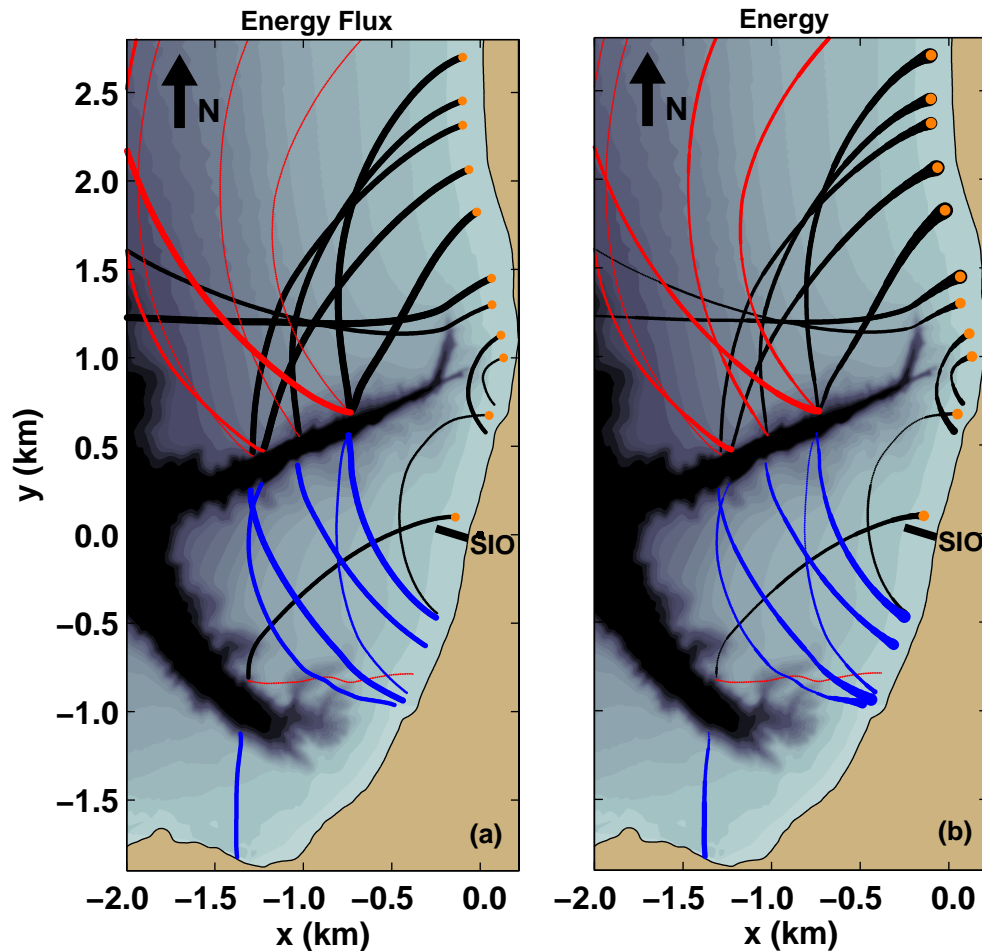


Figure 4-2: Ray paths (black curves) of 50 s period infragravity waves radiated seaward from the edge of the surfzone (2.5 m depth, orange dots) at $\theta_0 = -20^\circ$ from shore normal. The width of each ray path is scaled by (a) energy flux, which is conserved after initialization in 2.5 m depth, and (b) energy, which is proportional to $h^{-1/2}$ during refraction. Applying the long-wave theory verified in Chapter 3, energy flux (and corresponding ray width) is conserved when rays are divided into partially reflected (red curves) and transmitted (blue curves) paths at the canyons.

locations along the 2.5 m isobath. Ray paths are traced seaward from 2.5 m depth, and then summed over a 50-m resolution grid, assuming a linear superposition of the refracted wave components. Approximating the depth h as constant within each grid cell, the infragravity variance is calculated by summing contributions $\sum Fds(gh)^{-1/2}$ of ray segments passing thru each grid cell [Bouws and Battjes, 1982].

The modeled variance distribution is compared with the total infragravity variance observed at offshore instrument sites (grouped by depth for plotting, Figures 4-3 and 4-4). A normalized root-mean-square error ϵ (Eq. 3.19) is used to compare the modeled variance with the observed variance (Figure 4-5). The total variance is used because the dominant contributions to the shelf infragravity wave field are free waves (e.g., Figure 4-1) generated in the nearby surfzone. Additional free wave energy from remote sources (e.g., surfzones across the Pacific Ocean [Webb *et al.*, 1991]), as well as local group-bound contributions, are assumed to be small. Several grid resolutions (150, 100, 50, 25 m) and ray segment lengths ($ds = 5, 10, 20$ m) were tested, with the final 50 m grid and 5 m ray segment values chosen as the best combination of accuracy and computational efficiency. The results are insensitive to the type (e.g., linear, quadratic, cubic spline) of interpolation used for producing initial conditions.

4.2.1 Case Study

In a case study with narrow-banded directional spectra ($\theta_0 = -20 \pm 15^\circ$) radiated seaward from the surfzone, canyon effects (reflection and transmission) are important to the distribution of infragravity variance (Figure 4-3). If canyon effects are neglected (i.e., paths include refraction only), the energy flux along paths that intersect the canyon (e.g., Figure 4-2) is propagated southward along the coast (i.e., not reflected), and the resulting infragravity variance is overpredicted at most sites (Figure 4-3). Although as large as a factor of two in places (e.g., $y = 1100$ m on the 5 m isobath, Figure 4-3b), the overprediction typically is not severe because Scripps canyon is narrow (~ 100 m wide) relative to infragravity wavelengths (~ 500 m), and thus

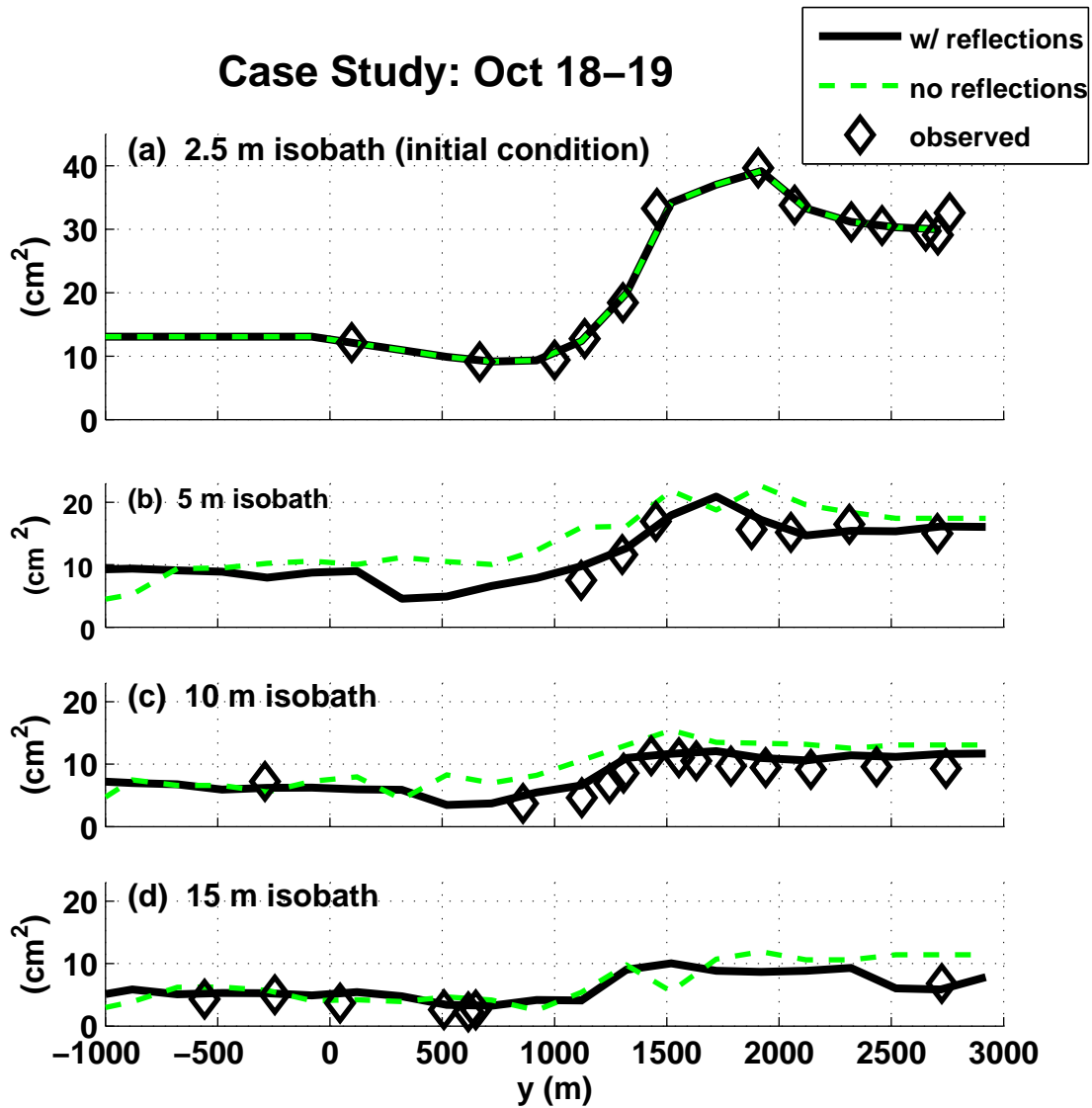


Figure 4-3: Observed (symbols) and modeled (curves) infragravity variance (cm^2) versus alongshore distance y (m) at four depths $h =$ (a) 2.5, (b) 5.0, (c) 10.0, (d) 15.0 m for 12 hrs spanning October 18-19, 2003. In this directionally narrow-banded case study, a ray tracing model that includes reflection and transmission at the canyons (solid black curves) has more skill than a refraction-only ray tracing model (dashed green curves). The models are initialized by interpolating the observations along the 2.5 m isobath (a) and radiating rays seaward according to the 12 hr averaged $\theta_0 = -20 \pm 15^\circ$ directional spectrum estimate, where θ is measured relative to shore normal.

modeled reflections are small ($< 30\%$) for most angles of incidence (Eq. 3.1). Likely, canyon effects would be more significant (e.g., reflections up to 95%) in the vicinity of the wider (~ 350 m) La Jolla Canyon, but there were only limited observations for comparison, and none for surfzone initialization, south of the Scripps Pier ($y < 0.0$ km, Figure 1-3).

4.2.2 Climatology

When averaging over almost two months of data to examine an approximate climatology of infragravity variance in the region surrounding Scripps canyon, the averaged directional spectrum radiated seaward from the surfzone (i.e., the initial condition) is broad and symmetric (average $\theta_0 = 0 \pm 60^\circ$), and the corresponding distribution from the ray tracing model is insensitive to canyon reflection effects (Figure 4-4). The alongshore gradients of infragravity energy, which are established in the surfzone by the incident swell energy, are reduced during the seaward propagation and unshoaling of a wave field with broad-band directional spectra (i.e., the curves in Figure 4-4 become flatter as water depth increases). Thus, the averaged distribution demonstrates only the indirect effect of the canyons, because refraction of incoming swell over the canyons affects the amount of energy available for infragravity wave generation, but does not affect the averaged outgoing infragravity wave propagation. Individual ray paths, however, can undergo significant reflections (e.g., Figure 4-2), and because energy propagating along individual ray paths could be important in forcing resonant seiche modes of harbors and bays, reflections should be included in models of broad-band wave propagation over steep bathymetry.

4.2.3 Model Skill

Comparisons of the observed infragravity variance with model simulations of variance indicate that reflection and transmission at the canyons are important near Scripps canyon (Figure 4-5a), but decrease in importance with distance from the canyons

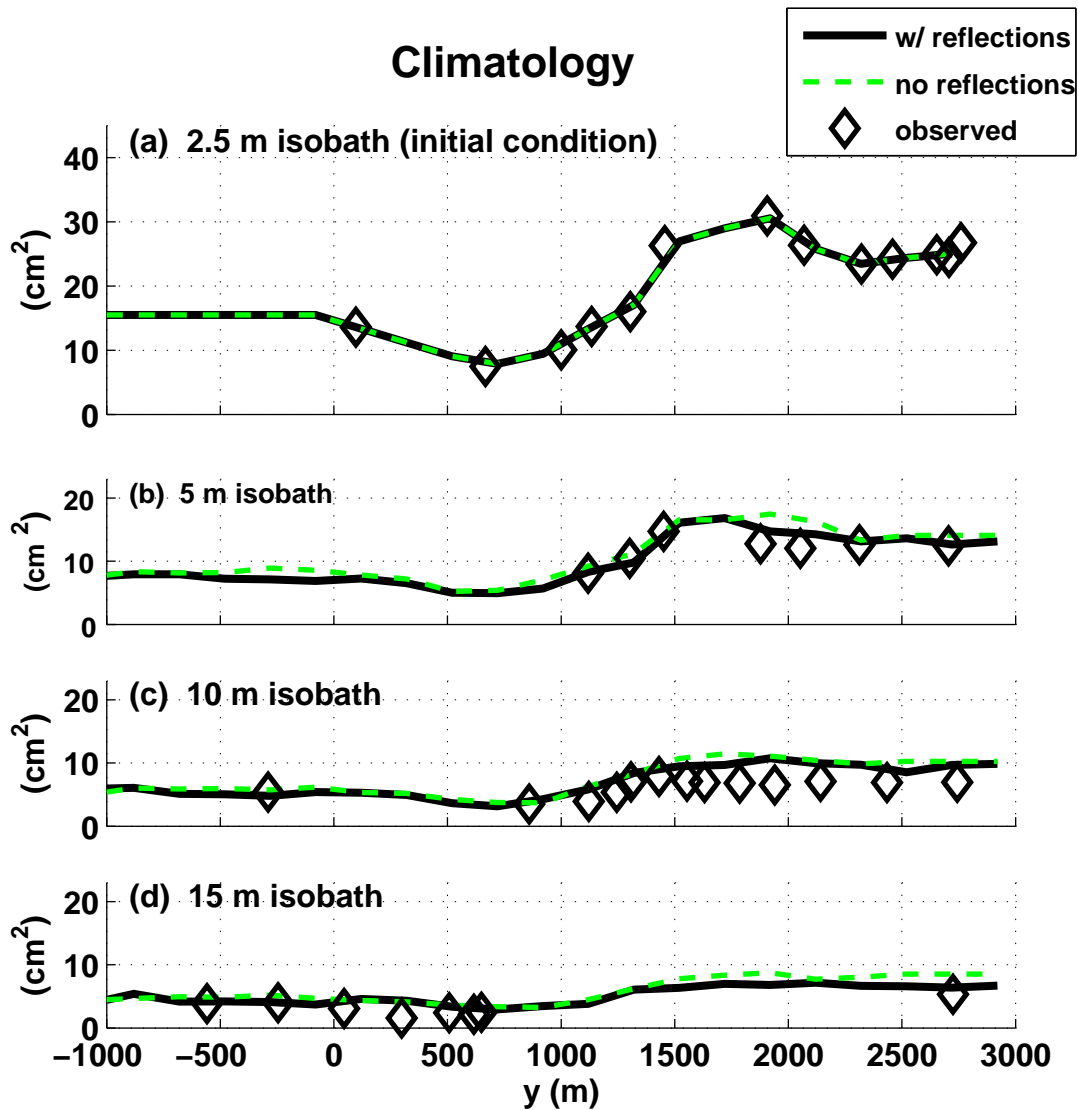


Figure 4-4: Average observed (symbols) and modeled (curves) infragravity variance (cm^2) versus alongshore distance y (m) at four isobaths $h =$ (a) 2.5, (b) 5.0, (c) 10.0, (d) 15.0 m for the entire Nearshore Canyon Experiment (fall 2003). Canyon effects are blurred when results are integrated over directionally broad-banded spectra. When initialized with an averaged frequency-directional spectrum, a ray tracing model that includes reflection and transmission at the canyons (solid black curves) has skill similar to that of a refraction-only ray tracing model (dashed green curves). The models are initialized by interpolating the average variance observed along the 2.5 m isobath (a) and radiating rays seaward according to an average $\theta = 0 \pm 60^\circ$ directional spectrum estimate, where θ is measured relative to shore normal. Averaging the results from all the individual cases using case-by-case initial conditions results in a similar description of the climatology.

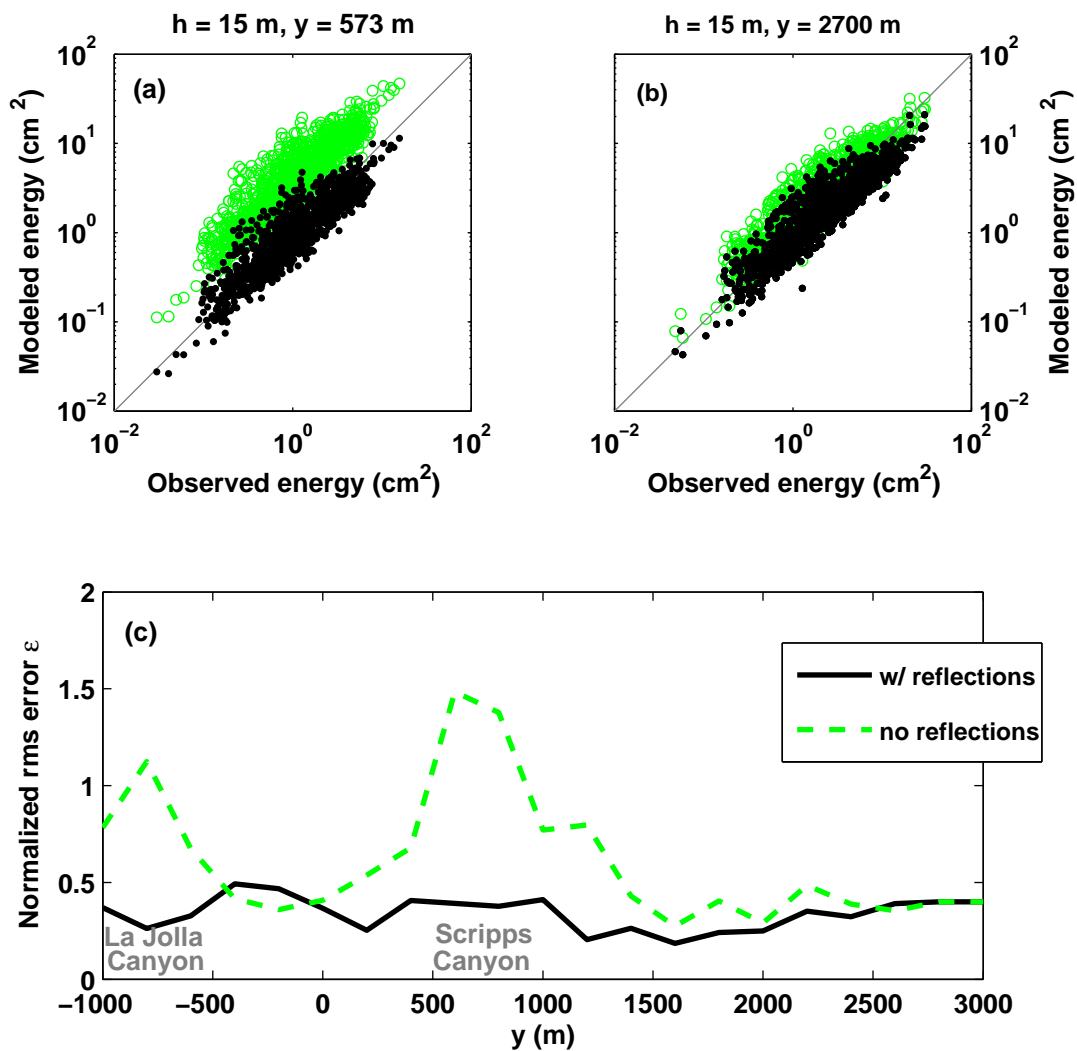


Figure 4-5: Modeled versus observed infragravity energy (cm^2) in 15-m water depth (a) near a canyon and (b) far from the canyons, and (c) normalized root-mean-square model errors versus alongshore distance. Results from the refraction model with canyon reflections (black filled circles) are scattered around a 1:1 agreement (gray lines) with observations at both locations (a and b). Results from the refraction model without canyon reflections (green open circles) agree with observations at locations far from the canyons (b), but not at locations near a canyon (a). The depth-averaged normalized root-mean-square error (c) is small along the entire array for the refraction model with canyon reflections (black curve), and large in the vicinity of the La Jolla and Scripps canyons for the refraction-only model (green dashed curve).

(Figure 4-5b). Averaging over all 1-hr records (1100 total) and all offshore instrument locations (40 total), including canyon effects in the refraction simulations results in improved model skill within one km (i.e., a few wavelengths) of the canyons, where the normalized model error remains small only if reflection and transmission are included (Figure 4-5c). On average, the refracted-reflected-transmitted ray tracing model explains 84% of the observed variance (defined as $100 \times [1 - \epsilon^2]$), while the refraction-only version explains 70% of the variance. Canyon reflection effects are found to be most significant for cases with narrow-banded initial directional spectra. For directionally broad-banded wave fields, the energy is spread more evenly over the ray paths at each grid cell, and the modeled variance distributions are similar with or without accounting for reflection and transmission at the canyons.

4.3 Suggested Applications

The results presented in this thesis can be used to improve the accuracy of nonlinear wave models in the surfzone and to extend the validity of linear wave models to regions of steep topography. The results could be incorporated into a comprehensive coastal wave model in which:

- swell waves are refracted shoreward from a single offshore measurement,
- infragravity wave energy is gained by nonlinear interactions in the shoaling region,
- infragravity wave energy is gained and lost by nonlinear interactions in the surfzone (including tidal modulations owing to variable beach slopes),
- the resulting total wave energy forces a nearshore circulation and corresponding sediment transport model,
- infragravity waves are reflected from the beach and radiated seaward,

- seaward rays are refracted and partially reflected over topography, and
- the resulting regional infragravity distribution forces bottom-pressure fluctuations (observed in seismic records) and possible harbor and bay resonances.

The improved predictions of infragravity waves within such a comprehensive model might be of use in coastal engineering and management applications. At present, the predictions of nearshore conditions that are used for recreational, commercial, or defense related sites are semi-empirical and remain prone to errors because of deficiencies in modeling the underlying physics. Infragravity wave dynamics must be understood before these models can predict nearshore waves, currents, and morphology accurately. For example, infragravity edge waves can support alongshore pressure gradients [Mei, 1989, § 4.8] that can force circulation patterns, including the episodic and hazardous seaward flows known as rip currents [MacMahan *et al.*, 2004]. In addition, infragravity motions dominate the run-up of water onto the beach face [Raubenheimer and Guza, 1996], and are associated with morphological features such as beach cusps [Ciriano *et al.*, 2005] and flooding during storms. Farther offshore, infragravity motions contaminate ocean bottom seismology measurements used to detect tsunamis [Mofjeld *et al.* 2001] and to predict microseisms [Rhie and Romanowicz, 2004].

In addition to modeling studies and predictive applications, future work might include investigations of submarine canyons as shoreline protection systems, possible feedbacks between tidal modulations and nearshore bottom profiles, the momentum balance associated with the reversal of nonlinear transfers in shallow water, and infragravity wave participation in the overall energy cascade to higher frequencies during surfzone wave breaking [Herbers *et al.*, 2000].

Bibliography

- Bouws, E. and J.A. Battjes (1982), A Monte Carlo approach to the computation of refraction of water waves, *J. Geophys. Res.*, *87*, C8 5718-5722.
- Ciriano, Y., G. Coco, K.R. Bryan, and S. Elgar (2005), Field observations of swash zone infragravity motions and beach cusp evolution, *J. Geophys. Res.*, *110*, C02018, doi:10.1029/2004JC002485.
- Elgar, S., T.H.C. Herbers, and R.T. Guza (1994), Reflection of ocean surface gravity waves from a natural beach, *J. Phys. Oceanogr.*, *24*, 1503-1511.
- Elgar, S., T.H.C. Herbers, M. Okihiro, J. Oltman-Shay, and R.T. Guza (1992), Observations of infragravity waves, *J. Phys. Oceanogr.*, *97*, C10 15573-15577.
- Guza, R.T., and E.B. Thornton (1985), Observations of surf beat, *J. Phys. Oceanogr.*, *90*, C2 3161-3172.
- Herbers, T.H.C, S. Elgar, and R.T. Guza (1995a), Infragravity-frequency (0.005-0.05 Hz) motions on the shelf, II, Free waves, *J. Phys. Oceanogr.*, *25*, 6, 1063-1079.
- Herbers, T.H.C, S. Elgar, and R.T. Guza (1995b), Generation and propagation of infragravity waves, *J. Phys. Oceanogr.*, *100*, C12 24863-24872.
- Herbers, T.H.C., N.R. Russnogle, and S. Elgar (2000), Spectral energy balance of breaking waves within the surf zone, *J. Phys. Oceanogr.*, *30*, 2723-2737.
- Longuet-Higgins, M.S. and R.W. Stewart (1962), Radiation stress and mass transport in surface gravity waves with application to surf beats, *J. Fluid Mech.*, *13*, 481-504.
- MacMahan, J.H., A.J.H.M. Reniers, E.B. Thornton, and T.P. Stanton (2004), Infragravity rip current pulsations, *J. Geophys. Res.*, *109*, C01033, doi:10.1029/2003JC002068.

- Mei, C.C. (1989), The Applied Dynamics of Ocean Surface Waves, *Adv. Series on Ocean Eng., Vol 1*, World Scientific, New Jersey, 740 pp.
- Mofjeld, H.O., P.M. Whitmore, M.C. Eble, F.I. Gonzalez, and J.C. Newman (2001), Seismic-wave contributions to bottom pressure fluctuations in the North Pacific Implications for the DART Tsunami Array, *Proc. Int. Tsunami Sym. 2001 (ITS 2001)*, Session 5-10, 633641.
- Munk, W.H. and Traylor, M.A. (1947), Refraction of ocean waves: a process linking underwater topography to beach erosion, *J. of Geology, LV*, 1-26.
- Oltman-Shay, J., and R.T. Guza (1987), Infragravity edge wave observations on two California beaches, *J. Phys. Oceanogr., 17*, 644-663.
- O'Reilly, W.C., and R.T. Guza (1993), A comparison of two spectral wave models in the Southern California Bight, *Coastal Eng., 19*, 263-282.
- Raubenheimer, B. and Guza, R.T. (1996), Observations and predictions of run-up, *J. Geophys. Res., 101*, C11 25575-25587.
- Reniers, A.J.H.M., J.H. MacMahan, E.B. Thornton, and T.P. Stanton (2006), Modelling infragravity motions on a rip-channel beach, *Coastal Eng., 53*, 209-222.
- Rhie, J. and B. Romanowicz (2004), Excitation of Earth's continuous free oscillations by atmosphere-ocean-seafloor coupling, *Nature, 431*, 552-556.
- Sheremet, A., R.T. Guza, S. Elgar, and T.H.C. Herbers (2002), Observations of nearshore infragravity waves: seaward and shoreward propagating components, *J. Geophys. Res., 107* (C8), 3095, doi:10.1029/2001JC000970.
- Thomson, J., S. Elgar, and T.H.C. Herbers (2005), Reflection and tunneling of ocean waves observed at a submarine canyon, *Geophys. Res. Lett., 32*, L10602, doi:10.1029/2005GL022834.

Thomson, J., S. Elgar, B. Raubenheimer, T.H.C. Herbers, and R.T. Guza (2006), Tidal modulation of infragravity waves via nonlinear energy losses in the surf-zone, *Geophys. Res. Lett.*, *33*, L05601, doi:10.1029/2005GL025514.

Webb, S., X. Zhang, and W. Crawford (1991), Infragravity waves in the deep ocean, *J. Geophys. Res.*, *96*, 2723-2736.